

Properties of Ly α emitters around the radio galaxy MRC 0316–257[★]

B. P. Venemans¹, H. J. A. Röttgering¹, G. K. Miley¹, J. D. Kurk², C. De Breuck³, R. A. Overzier¹, W. J. M. van Breugel⁴, C. L. Carilli⁵, H. Ford⁶, T. Heckman⁶, L. Pentericci⁷, and P. McCarthy⁸

¹ Sterrewacht Leiden, P.O. Box 9513, 2300 RA, Leiden, The Netherlands

² INAF, Osservatorio Astrofisico di Arcetri, Largo Enrico Fermi 5, 50125, Firenze, Italy

³ European Southern Observatory, Karl Schwarzschild Straße 2, D-85748 Garching, Germany

⁴ Lawrence Livermore National Laboratory, P.O. Box 808, Livermore CA, 94550, USA

⁵ NRAO, P.O. Box 0, Socorro NM, 87801, USA

⁶ Dept. of Physics & Astronomy, The Johns Hopkins University, 3400 North Charles Street, Baltimore MD, 21218-2686, USA

⁷ Dipartimento di Fisica, Università degli studi Roma Tre, Via della Vasca Navale 84, Roma, 00146, Italy

⁸ The Observatories of the Carnegie Institution of Washington, 813 Santa Barbara Street, Pasadena CA, 91101, USA

Received 21 September 2004; accepted 21 October 2004

Abstract. Observations of the radio galaxy MRC 0316–257 at $z = 3.13$ and the surrounding field are presented. Using narrow- and broad-band imaging obtained with the VLT, 77 candidate Ly α emitters with a rest-frame equivalent width of $> 15 \text{ \AA}$ were selected in a $\sim 7' \times 7'$ field around the radio galaxy. Spectroscopy of 40 candidate emitters resulted in the discovery of 33 emission line galaxies of which 31 are Ly α emitters with redshifts similar to that of the radio galaxy, while the remaining two galaxies turned out to be [O II] emitters. The Ly α profiles have widths (*FWHM*) in the range of 120–800 km s^{-1} , with a median of 260 km s^{-1} . Where the signal-to-noise was large enough, the Ly α profiles were found to be asymmetric, with apparent absorption troughs blueward of the profile peaks, indicative of absorption along the line of sight of an H I mass of at least $2 \times 10^2 - 5 \times 10^4 M_{\odot}$. Besides that of the radio galaxy and one of the emitters that is a QSO, the continuum of the emitters is faint, with luminosities ranging from $1.3 L^*$ to $< 0.03 L^*$. The colors of the confirmed emitters are, on average, very blue. The median UV continuum slope is $\beta = -1.76$, bluer than the average slope of LBGs with Ly α emission ($\beta \sim -1.09$). A large fraction of the confirmed emitters ($\sim 2/3$) have colors consistent with that of dust-free starburst galaxies. Observations with the Advanced Camera for Surveys on the *Hubble Space Telescope* show that the emitters that were detected in the ACS image have a range of different morphologies. Four Ly α emitters ($\sim 25\%$) were unresolved with upper limits on their half light radii of $r_h < 0.6 - 1.3 \text{ kpc}$, three objects ($\sim 19\%$) show multiple clumps of emission, as does the radio galaxy, and the rest ($\sim 56\%$) are single, resolved objects with $r_h < 1.5 \text{ kpc}$. A comparison with the sizes of Lyman break galaxies at $z \sim 3$ suggests that the Ly α emitters are on average smaller than LBGs. The average star formation rate of the Ly α emitters is $2.6 M_{\odot} \text{ yr}^{-1}$ as measured by the Ly α emission line or $< 3.9 M_{\odot} \text{ yr}^{-1}$ as measured by the UV continuum. The properties of the Ly α galaxies (faint, blue and small) are consistent with young star forming galaxies which are still nearly dust free.

The volume density of Ly α emitting galaxies in the field around MRC 0316–257 is a factor of $3.3^{+0.5}_{-0.4}$ larger compared with the density of field Ly α emitters at that redshift. The velocity distribution of the spectroscopically confirmed emitters has a dispersion of 640 km s^{-1} , corresponding to a *FWHM* of 1510 km s^{-1} , which is substantially smaller than the width of the narrow-band filter (*FWHM* $\sim 3500 \text{ km s}^{-1}$). The peak of the velocity distribution is located within 200 km s^{-1} of the redshift of the radio galaxy. We conclude that the confirmed Ly α emitters are members of a protocluster of galaxies at $z \sim 3.13$. The size of the protocluster is unconstrained and is larger than $3.3 \times 3.3 \text{ Mpc}^2$. The mass of this structure is estimated to be $> 3-6 \times 10^{14} M_{\odot}$ and could be the progenitor of a cluster of galaxies similar to e.g. the Virgo cluster.

Key words. Galaxies: active — Galaxies: high-redshift — Galaxies: evolution — Galaxies: clusters: general — Cosmology: observations — Cosmology: early Universe

1. Introduction

Within Cold Dark Matter (CDM) scenarios the first stars and stellar systems form through gravitational infall of primordial gas in large CDM halos (e.g. White & Rees, 1978). Numerical simulations suggest that as these halos merge they form vast, web-like networks of young galaxies and ionized gas (e.g.

Send offprint requests to: B. P. Venemans (venemans@strw.leidenuniv.nl)

* Based on observations carried out at the European Southern Observatory, Paranal, Chile, programs LP167.A-0409 and 68.B-0295.

Baugh et al., 1998). The most massive galaxies, and the richest clusters emerge from regions with the largest overdensities. Although clusters of galaxies have been studied extensively out to $z \sim 1.3$ (e.g. Rosati et al., 1999; Della Ceca et al., 2000; Stanford et al., 2002; Blakeslee et al., 2003b; Maughan et al., 2003; Toft et al., 2004), the epoch of cluster formation is still an open question due to the difficulty in identifying their progenitors in the early Universe.

During the last decade, evidence has mounted that the most powerful high redshift radio galaxies (HzRGs; $z > 2$) are progenitors of brightest cluster galaxies and are located in dense environments. HzRGs are amongst the brightest and presumably most massive galaxies (Jarvis et al., 2001; De Breuck et al., 2002; Zirm et al., 2003). They have high star formation rates ($> 100 M_{\odot} \text{ yr}^{-1}$), based on deep spectra of their UV continuum (e.g. Dey et al., 1997) and the detections of dust (e.g. Archibald et al., 2001; Stevens et al., 2003; Reuland et al., 2004) and extended CO emission (Papadopoulos et al., 2000; De Breuck et al., 2003a,b). Furthermore, radio galaxies at redshifts between 0.5 and 1.5 are known to predominantly lie in moderately rich clusters (Hill & Lilly, 1991; Best, 2000; Best et al., 2003). At higher redshifts ($z > 2$), some radio galaxies were found to possess companion galaxies (Le Fèvre et al., 1996; Pascarelle et al., 1996; Röttgering et al., 1996; Keel et al., 1999). Also, 20% of the HzRGs have extreme radio rotation measures ($> 1000 \text{ rad m}^{-2}$), giving an indication that these radio galaxies are surrounded by dense hot gas (Carilli et al., 1997; Athreya et al., 1998; Pentericci et al., 2000b).

To search for direct evidence of the association of a cluster or a forming cluster (protocluster) with a radio galaxy, we conducted a pilot project on the Very Large Telescope (VLT) aimed at finding an excess of Ly α emitters around the clumpy radio galaxy PKS 1138–262 at $z = 2.16$. Narrow-band imaging resulted in a list of ~ 50 candidate Ly α emitters (Kurk et al., 2000, 2004). Subsequent multi-object spectroscopy confirmed 14 Ly α emitting galaxies and one QSO whose velocities were within 1000 km s^{-1} of the central radio galaxy (Pentericci et al., 2000a; Kurk et al., 2004). The volume density of Ly α emitters near PKS 1138–262 was found to be a factor 4.4 ± 1.2 times that of Ly α emitters in blank fields (Kurk et al., 2004). Using near-infrared narrow- and broad-band images of the field, significant populations of H α emitters at the redshift of the radio galaxy and extremely red objects were found. Also, *Chandra* observations revealed an excess of soft X-ray sources in the field of PKS 1138–262 (Pentericci et al., 2002), indicating that several AGN are present in the protocluster.

As shown by the study of the overdense region near PKS 1138–262, distant protoclusters provide ideal laboratories for tracing the development of large scale structure and galaxy evolution. To further study the formation of large scale structure in the early Universe and to investigate the evolution of galaxies in dense environments, we initiated a large program on the VLT to search for Ly α emitting galaxies around luminous radio galaxies with redshifts $2 < z < 5$ (Venemans et al., 2003). The goals were to find protoclusters of galaxies, determine the fraction of HzRGs associated with protoclusters and study the properties of protoclusters and their galaxies. The first result

was the discovery of a protocluster around the radio galaxy TN J1338–1942 at $z = 4.1$ (Venemans et al., 2002). Deep imaging and spectroscopy revealed 20 Ly α emitters within a projected distance of 1.3 Mpc and 600 km s^{-1} of the radio galaxy. By comparing the density of Ly α emitters in the protocluster to the field, the galaxy overdensity was claimed to be 4.0 ± 1.4 and the mass of the structure was estimated to be $\sim 10^{15} M_{\odot}$ (Venemans et al., 2002).

Here we report on observations of the radio galaxy MRC 0316–257. This 1.5 Jy radio source was listed in the 408 MHz Molonglo Reference Catalogue (Large et al., 1981) and optically identified by McCarthy et al. (1990). Its discovery spectrum yielded a redshift of 3.13 (McCarthy et al., 1990). This object was included in our program because the redshift of the radio galaxy shifted the Ly α line into one of the narrow-band imaging filters available at the VLT. Also, it already had two spectroscopically confirmed Ly α emitting companions (Le Fèvre et al., 1996, hereafter LF96), an indication that the radio galaxy is located in a dense environment. Further, the redshift of the radio galaxy of 3.13 allows for an efficient search for Lyman Break Galaxies (LBGs) and for [O III] $\lambda 5007 \text{ \AA}$ emitters using a K-band narrow-band filter, which is available in the Infrared Spectrometer and Array Camera (ISAAC, Moorwood, 1997) at the VLT.

Besides observing MRC 0316–257 with the VLT as part of our large program, we made additional observations of the field with the Advanced Camera for Surveys (ACS; Ford et al., 1998) on the *Hubble Space Telescope (HST)*¹ to study the sizes and morphologies of the detected galaxies.

This paper is organized in the following way. In Sect. 2 the imaging observations and data reduction are described and Sect. 3 discusses how candidate Ly α emitters in the field are detected. The spectroscopic observations and the results are presented in Sect. 4. The properties of the Ly α emitters are analyzed in Sect. 5, and details of individual emitters are presented in Sect. 6. Evidence for the presence of a protocluster in the field is discussed in Sect. 7, and the properties are presented in Sect. 8. In Sect. 9 the nature of the Ly α emitters is discussed, followed by a description of the implications of a protocluster at $z = 3.13$ in Sect. 10.

Throughout this article, magnitudes are in the AB system (Oke, 1974), using the transformations $V_{\text{AB}} = V_{\text{Vega}} + 0.01$ and $I_{\text{AB}} = I_{\text{Vega}} + 0.39$ (Bessell, 1979). A Λ -dominated cosmology with $H_0 = 65 \text{ km s}^{-1} \text{ Mpc}^{-1}$, $\Omega_M = 0.3$, and $\Omega_{\Lambda} = 0.7$ is assumed. In this cosmology, the luminosity distance of MRC 0316–257 is 28.8 Gpc and $1''$ corresponds to 8.19 kpc at $z = 3.13$.

¹ Based on observations made with the NASA/ESA Hubble Space Telescope, obtained at the Space Telescope Science Institute, which is operated by the Association of Universities for Research in Astronomy, Inc., under NASA contract NAS 5-26555. These observations are associated with program #8183

Table 1. Summary of the observations of the field around MRC 0316–257.

Date	Telescope	Instrument	Mode	Optical element	Seeing	Exposure time
2001, September 20 and 21	VLT UT4	FORS2	Imaging	Bessel <i>V</i>	0".7	4 860 s
2001, September 20 and 21	VLT UT4	FORS2	Imaging	OIII/3000	0".7	23 400 s
2001, September 22	VLT UT4	FORS2	MOS ^a	GRIS_1400V	~ 1".5	12 600 s
2001, October 18	VLT UT4	FORS2	MXU ^b , mask I	GRIS_1400V	1".0	10 800 s
2001, October 18, 19 and 20	VLT UT4	FORS2	MXU ^b , mask II	GRIS_1400V	1".0	29 100 s
2001, November 15 and 16	VLT UT3	FORS1	PMOS ^c	GRIS_300V	0".8	19 800 s
2002, July 18	<i>HST</i>	ACS	Imaging	F814W	–	6300 s
2002, September 6, 7 and 8	VLT UT4	FORS2	Imaging	Bessel <i>I</i>	0".7	4 680 s

^a Multi-object spectroscopy mode, performed with 19 movable slitlets with lengths of 20"–22".

^b Multi-object spectroscopy mode with a user-prepared mask.

^c Spectropolarimetry mode using 9 movable slitlets of 20".

2. Imaging observations and data reduction

2.1. VLT imaging

An overview of the observations is shown in Table 1. On 2001, September 20 and 21, narrow- and broad-band imaging was carried out with the 8.2 m Yepun (VLT UT4) to search for Ly α emitting galaxies around MRC 0316–257. The instrument used was the FOcal Reducer/low dispersion Spectrograph 2 (FORS2; Appenzeller & Rupprecht, 1992) in imaging mode. For the narrow-band imaging the OIII/3000 filter was used with a central wavelength of 5045 Å and full width half maximum (*FWHM*) of 59 Å, which samples the Ly α line from the radio galaxy, which is redshifted to 5021 Å (McCarthy et al., 1990, LF96). To measure the UV continuum near the Ly α line, the field was imaged with broad-band filter Bessel *V* with a central wavelength of 5540 Å and *FWHM* of 1115 Å. The detector was a SiTE CCD with 2048×2048 pixels. The pixel scale was 0".2 per pixel, resulting in a field of view of 6'.8×6'.8. A year later, on 2002, September 6, 7 and 8, broad-band images of the field were taken in the Bessel *I* filter, with a central wavelength of 7680 Å and a *FWHM* of 1380 Å. The instrument was again FORS2, but the detector was replaced by two MIT CCDs with 2048×2048 pixels each. The gap between the two CCDs was ~ 4 arcsec. The pixel scale of the MIT CCDs was 0".125 per pixel. To decrease the readout time, the pixels were binned by 2 × 2, resulting in a spatial scale of 0".25 pixel⁻¹. The field of view was restricted by the geometry of the Multi-Object Spectroscopy (MOS) unit, and was 6'.8×6'.8.

The observations in the narrow-band were split into 13 separate exposures of 1800 s, in *V*-band into 27 separate 180 s exposures and in the *I*-band 26 exposures of 180 s were taken. The individual exposures were shifted by ~ 15" with respect to each other to facilitate identifying cosmic rays and removing residual flat-field errors.

All nights except for 2001, September 20 were photometric, and the average seeing was 0".65 - 0".7 in the narrow-band, *V* and *I* images (see Table 1). For the flux calibration, the spectrophotometric standard star LTT 1788 (Stone & Baldwin, 1983; Baldwin & Stone, 1984) was observed in the *V*-band and the photometric standard stars in the field SA98 (Landolt, 1992) were used to calibrate the *I*-band images.

2.2. Data reduction of VLT data

The VLT images were reduced using standard routines within the reduction software package IRAF². The reduction steps included bias subtraction, flat fielding using twilight sky flats and illumination correction using the unregistered science frames.

The magnitude zero-points derived from different standard stars were consistent with each other within 0.02 magnitude. To derive the zero-point of the narrow-band image, the magnitude of the ~ 400 brightest objects in the field were measured in the *V* and *I*-band images. These objects had a signal-to-noise of at least 25 in both *V* and *I*-band images. A magnitude limit of $m_I > 20$ was set to reject saturated stars. Narrow-band magnitudes were derived from the *V* and *I*-band magnitudes assuming a powerlaw spectral energy distribution for these 400 objects. With these derived narrow-band magnitudes and the associated counts in the narrow-band image, the zero-point of the narrow-band image was computed. The rms of the computed zero-point was 0.006 mag.

All magnitudes were corrected for galactic extinction which was estimated by Schlegel et al. (1998) to have a value of $E(B - V) = 0.014$ mag. The measured 1 σ limiting magnitudes per square arcsecond were 28.35, 28.90 and 28.69 for the narrow-band, *V*-band and *I*-band respectively.

Astrometric calibration was performed using the USNO-A2.0 catalog (Monet et al., 1998; Monet, 1998) from which 20 stars were identified in the field. This resulted in a fit with a typical error in the right ascension and declination of 0".17. The astrometric accuracy of the images is dominated by the uncertainty of the USNO-A2.0 catalog of 0".25 (Deutsch, 1999). The VLT images were registered in the following way. Because the *V*-band and narrow-band images were taken with the same detector, a simple pixel shift was sufficient to align the images, using the positions of a few stars over the field. The *I*-band frames were taken with the MIT CCDs, which had a different pixel scale (0".25 pixel⁻¹) as compared to the SiTE CCD (0".2 pixel⁻¹). The distortions were also different, and rescaling the *I*-band image to the same pixel scale as the *V*-band

² IRAF is distributed by the National Optical Astronomy Observatories, which are operated by the Association of Universities for Research in Astronomy, Inc., under cooperative agreement with the National Science Foundation.

image resulted in positional errors up to a few arcseconds in the corners of the I -band image. Instead, the position of a few hundred objects detected in both the I -band and V -band images with a signal-to-noise greater than 15, were used for the alignment. This way the positional error of objects in the I -band image dropped to $0''.04$. Subsequently, the algorithm DRIZZLE (Fruchter & Hook, 2002) was used to map the I , V and narrow-band images on new frames with a common pixel scale of $0''.16$.

The area of the reduced images was 46.7 arcmin^2 . Due to the presence of two bright stars in the field, the area that could be used for detecting candidate Ly α emitters was 45.75 arcmin^2 . The width of the narrow-band filter in redshift is 0.049 at $z \sim 3.13$ and the volume probed by the filter at $z = 3.13$ is 9331 Mpc^3 .

2.3. Hubble Space Telescope imaging and reduction

A part of the field imaged by the VLT was observed in 2002 July with the ACS on board the *HST* as part of an imaging program of HzRGs. The $3'.4 \times 3'.4$ field of view of the ACS was chosen to include not only the radio galaxy but also as many confirmed Ly α emitters as possible (see Fig. 14 for the position of the ACS field within the FORS field). The field was imaged in the F814W filter (hereafter I_{814}) with a central wavelength of 8333 \AA and a width of 2511 \AA . The total exposure time was 6300 s. The images were reduced using the ACS GTO pipeline (Blakeslee et al., 2003a).

3. Detection and selection of candidate emitters

3.1. Source detection

For the detection and photometry of objects in the images, the program SExtractor (version 2.2.2, Bertin & Arnouts, 1996) was applied. The narrow-band image was used to detect the objects. Because some of the Ly α emitters remained undetected in the broad-band images (see Table 4), this was preferred above a combination of the narrow-band and broad-band images as detection image, which is favoured by some other groups (e.g. Fynbo et al., 2002). Detected objects in the narrow-band image were defined to have at least 15 connected pixels with values larger than the rms sky noise. This resulted in a list of 3505 objects, of which 3209 had a signal-to-noise greater than five. To assess the completeness of the catalog, artificial and real galaxies were added to the narrow-band image and recovered. The galaxies had various sizes, the smallest galaxies had a half light radius $r_h \sim 0.4''$, similar to that of stars in the field (unresolved objects), the largest galaxies had a half light radius $r_h \sim 0.9''$, roughly 2.5 times that of stars. We found that the completeness depended on the size of the galaxies that were added to the image as shown in Fig. 1. The limit where half of the galaxies were recovered ranged from a magnitude of $m_{\text{nb}} \lesssim 26.25$ for unresolved objects to $m_{\text{nb}} \lesssim 25.25$ for the largest objects. The 90% recovery limit was $m_{\text{nb}} \sim 26.0$ for unresolved and $m_{\text{nb}} \sim 25.0$ for the largest objects.

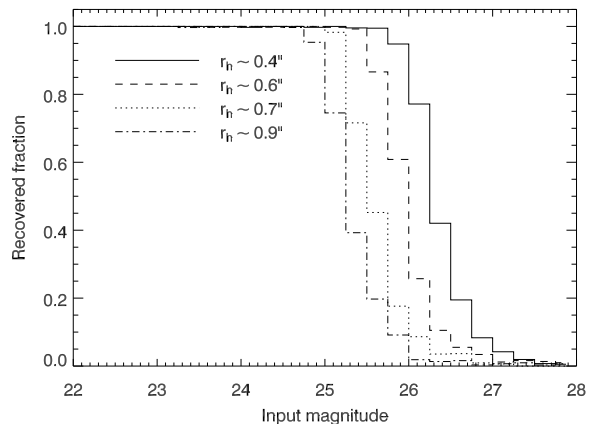


Fig. 1. Fraction of galaxies recovered in the narrow-band image versus magnitude for various galaxy sizes.

3.2. Photometry

To measure the flux of the detected objects, the double image mode of SExtractor was employed. In this mode, SExtractor detects objects in one image, and carries out the photometry on a second image. In our case, the narrow-band image was used for the detection of the objects and the photometry was done on the narrow-band and broad-band images. Of each detected object in the narrow-band the flux was measured in two apertures: a circular aperture to compute the colors of the object, and an elliptical aperture to estimate the total brightness of the object. The radius of the circular aperture (R_{aper}) depended on the isophotal area of the object (A_{iso}), which is the area of pixels with values above the rms sky noise and is an output parameter of SExtractor: $R_{\text{aper}} = \sqrt{A_{\text{iso}}/\pi}$. A minimum aperture radius of $0''.525$, 1.5 times the radius of the seeing disc, was set to avoid very small apertures. The maximum radius was set to 4 times the radius of the seeing disc to avoid overlapping apertures due to neighbouring galaxies. The shape and size of the elliptical aperture was derived from the object's light distribution. The ellipticity ε and position angle of the object were computed from the second order moment of the light distribution. Using the first moment r_1 , the elliptical aperture had major and minor axes of kr_1/ε and εkr_1 (Bertin & Arnouts, 1996). The scaling factor k determines the size of aperture and is a free parameter in SExtractor. We tested SExtractor on a set of images and compared SExtractor's output magnitudes for values of k in the range $1.0 < k < 2.75$. It was found that a scaling factor of $k \approx 1.75$ both optimized the signal-to-noise and minimized the fraction of the flux of the object outside the aperture.

The aperture used to measure the total flux of an object was the elliptical aperture, except when more than 10% of the pixels in the elliptical aperture was significantly effected by bright and close neighbours (SExtractor output parameter FLAGS equals 1) or when the object was originally blended with another one (FLAGS equals 2). In those cases the circular aperture was used to derive the total flux.

To estimate the fraction of the total flux of the object falling outside the (elliptical) aperture, Monte Carlo simulations were

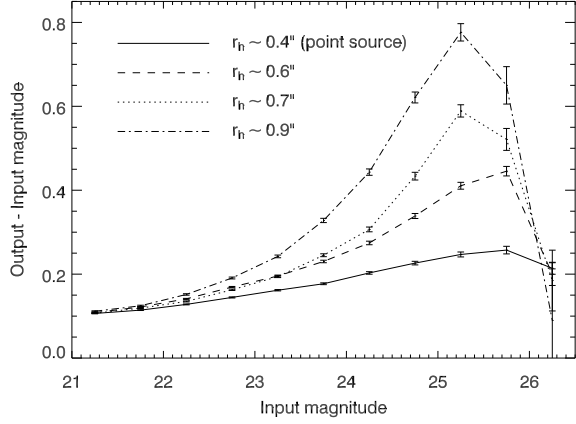


Fig. 2. Difference between measured magnitude and input magnitude as a function of input magnitude for objects with various sizes. The difference is larger for fainter and/or larger objects.

performed. Galaxies in the magnitude range $21 < m_{nb} < 28$ with various shapes (Gaussian and elliptical profiles) and sizes (half light radii $0.4'' < r_h < 0.9''$) were added to the narrow-band image and recovered. The number of galaxies added to the image was limited to 40 to avoid overcrowding. This routine was repeated until 8000 galaxies per magnitude bin were simulated. By comparing the measured magnitudes to the input magnitude of the simulated galaxies, the fraction of the flux that was outside the aperture could be estimated to correct the aperture magnitudes. The simulations showed that this fraction depends on both the original size of object and the magnitude of the object: the fraction of the flux outside the aperture is higher for a large and/or faint object, compared to a compact and/or bright object (see Fig. 2). At faint magnitudes the correction becomes smaller again, because these objects have a larger probability to be detected if they coincide with a peak in the noise. For the brightest objects the fraction of the flux outside the aperture is constant at a value of $\sim 11\%$. To avoid an overestimation of the magnitude correction, we decided to use only point sources to measure the correction (see Fig. 2). The magnitude correction applied to the sources in our field was $\lesssim 0.1$ for objects with $m_{nb} \lesssim 21$, rising to ~ 0.25 for objects with $m_{nb} \sim 26$.

3.3. Selection of candidate Ly α emitters

An efficient method of detecting Ly α emitting galaxies at high redshift is to select objects with a large line equivalent width (e.g. Cowie & Hu, 1998) using the narrow- and broad-band photometry. The observed equivalent width EW_{obs} of a Ly α line is defined as:

$$EW_{obs} = F_{Ly\alpha} / C_{Ly\alpha} \quad (1)$$

with $F_{Ly\alpha}$ the flux of the Ly α line and $C_{Ly\alpha}$ the UV continuum at the wavelength of the Ly α line. Assume that a Ly α line is observed in both a narrow-band filter and a broad-band filter, then the flux density in the narrow-band ($f_{\lambda,nb}$) and broad-band ($f_{\lambda,bb}$) can be described as:

$$f_{\lambda,nb} = C(\lambda = \lambda_{eff,nb}) + F_{Ly\alpha} / \Delta\lambda_{nb} \quad (2)$$

$$f_{\lambda,bb} = C(\lambda = \lambda_{eff,bb}) + F_{Ly\alpha} / \Delta\lambda_{bb}, \quad (3)$$

where C is the UV continuum and $\Delta\lambda_{bb(nb)}$ is the width of broad-band (narrow-band) filter (Eq. 5) and $\lambda_{eff,bb(nb)}$ the effective wavelength of broad-band (narrow-band) filter (Eq. 4).

The effective wavelength of a filter with transmission curve $T(\lambda)$ is given by

$$\lambda_{eff} = \frac{\int \lambda T(\lambda) d\lambda}{\int T(\lambda) d\lambda} \quad (4)$$

and the width of the filter $\Delta\lambda$ by

$$\Delta\lambda = \int T(\lambda) d\lambda / T_{max}, \quad (5)$$

with T_{max} the peak transmission of the filter. For a top-hat filter, the effective wavelength is equal to the central wavelength, the width equals the $FWHM$.

If the central wavelengths of the narrow-band and broad-band filters are roughly equal and the Ly α line falls in the centre of the filters, then eliminating either C or $F_{Ly\alpha}$ by substituting Eq. (2) in Eq. (3) gives:

$$F_{Ly\alpha} = \frac{\Delta\lambda_{bb}\Delta\lambda_{nb}(f_{\lambda,nb} - f_{\lambda,bb})}{\Delta\lambda_{bb} - \Delta\lambda_{nb}} \quad (6)$$

$$C_{Ly\alpha} = \frac{\Delta\lambda_{bb}f_{\lambda,bb} - \Delta\lambda_{nb}f_{\lambda,nb}}{\Delta\lambda_{bb} - \Delta\lambda_{nb}}, \quad (7)$$

and using Eq. (1) results in an expression for EW_{obs} :

$$EW_{obs} = \frac{\Delta\lambda_{bb}\Delta\lambda_{nb}(f_{\lambda,nb} - f_{\lambda,bb})}{\Delta\lambda_{bb}f_{\lambda,bb} - \Delta\lambda_{nb}f_{\lambda,nb}} \quad (8)$$

(e.g. Bunker et al., 1995; Malhotra & Rhoads, 2002). Alternatively, Eq. (8) can be used if it is expected that the fraction of the continuum flux falling in the filters that is absorbed by foreground H I is comparable to the fraction of the Ly α line that is extinguished by intergalactic absorption (as assumed by e.g. Malhotra & Rhoads, 2002).

If the central wavelengths of the narrow-band and broad-band filters differ, as is the case with our filters, then the slope of the UV continuum is needed to extrapolate the continuum strength from the central wavelength of the broad-band to the central wavelength of the narrow-band. Including an extra broad-band contribution redward of the Ly α line, the continuum slope can be calculated as well. Below is described how the equivalent width of a $z = 3.13$ Ly α emitter can be computed using our available photometry.

Assume that a Ly α emitter has a spectral energy distribution that consists of a Ly α line with flux $F_{Ly\alpha}$ and a UV continuum redward of the Ly α line with strength C and powerlaw slope β ($f_{\lambda} \propto \lambda^{\beta}$). The flux density in the narrow-band ($f_{\lambda,nb}$), V-band ($f_{\lambda,V}$) and I-band ($f_{\lambda,I}$) can then be characterized as:

$$f_{\lambda, \text{nb}} = Q_{\text{nb}} C \lambda_{\text{eff, nb}}^{\beta} + \epsilon_{\text{nb}} F_{\text{Ly}\alpha} / \Delta\lambda_{\text{nb}} \quad (9)$$

$$f_{\lambda, \text{V}} = Q_{\text{V}} C \lambda_{\text{eff, V}}^{\beta} + \epsilon_{\text{V}} F_{\text{Ly}\alpha} / \Delta\lambda_{\text{V}} \quad (10)$$

$$f_{\lambda, \text{I}} = C \lambda_{\text{eff, I}}^{\beta} \quad (11)$$

with $\lambda_{\text{eff, nb/V/I}}$ the effective wavelength corresponding to the narrow-band, V and I filter respectively (Eq. 4), $\Delta\lambda$ the width of the filter (Eq. 5), ϵ the efficiency of the filter at the wavelength of the redshifted Ly α line and Q the fraction of the continuum flux falling in the filter that is absorbed by the Ly α forest (Eq. 12). It should be mentioned that, in contrast to Eq. (8), no correction factor for foreground absorption of the Ly α line is applied in this calculation. If foreground extinction of the Ly α line is taken into account, then the equivalent width and Ly α line flux will be higher by $\sim 60\%$ (see Eq. 13).

For the filters (and instrument) used in this project, the input parameters are: $\lambda_{\text{eff, nb}} = 5040.1 \text{ \AA}$, $\Delta\lambda_{\text{nb}} = 61.1 \text{ \AA}$, $\lambda_{\text{eff, V}} = 5561.9 \text{ \AA}$, $\Delta\lambda_{\text{V}} = 1145.6 \text{ \AA}$ and $\lambda_{\text{eff, I}} = 7946.5 \text{ \AA}$. The efficiency ϵ of the filters depends on the redshift of the Ly α line. For all objects a redshift of $z = 3.13$ is assumed, and the efficiencies are $\epsilon_{\text{nb}} = 0.76$ and $\epsilon_{\text{V}} = 0.74$. It should be stressed that the computed equivalent width does not depend strongly on the assumed redshift in the interval $z = 3.13 - 3.17$. Assuming a redshift of $z = 3.12$ will yield equivalent widths that are a factor of ~ 2 higher compared to the equivalent widths computed with $z = 3.13$.

The fraction of the continuum flux that is absorbed by foreground neutral hydrogen averaged over the bandpass is Q :

$$Q = \frac{\int e^{-\tau_{\text{eff}}} T(\lambda) d\lambda}{\int T(\lambda) d\lambda} \quad (12)$$

where τ_{eff} is the effective opacity of H I. For observed wavelengths between the redshifted Ly α and redshifted Ly β line ($\lambda_{\text{Ly}\beta}(1+z) < \lambda_{\text{obs}} < \lambda_{\text{Ly}\alpha}(1+z)$), the expression for τ_{eff} that has been taken is:

$$\tau_{\text{eff}} = 0.0036 \left(\frac{\lambda_{\text{obs}}}{1216 \text{ \AA}} \right)^{3.46} \quad (13)$$

(Press et al., 1993; Madau, 1995). Because the Ly α line of an object at $z = 3.13$ falls in the blue wing of the V filter, the fraction of the continuum flux falling in the V filter that is absorbed is small and Q is near unity: $Q_{\text{V}} \sim 0.97$. In the narrow-band, $Q_{\text{nb}} = 0.92$ for a source at $z = 3.13$.

To calculate the equivalent width of an individual Ly α line, Eqs. (9) – (11) were solved for β , C and $F_{\text{Ly}\alpha}$. This was done in the following way. Equation (9) was multiplied by $\Delta\lambda'_{\text{nb}} = \Delta\lambda_{\text{nb}}/\epsilon_{\text{nb}}$ and Eq. (10) by $\Delta\lambda'_{\text{V}} = \Delta\lambda_{\text{V}}/\epsilon_{\text{V}}$. Substituting $C = f_{\lambda, \text{I}}/\lambda_{\text{eff, I}}^{\beta}$ (Eq. 11) gave:

$$\Delta\lambda'_{\text{nb}} f_{\lambda, \text{nb}} = f_{\lambda, \text{I}} \Delta\lambda'_{\text{nb}} Q_{\text{nb}} \left(\frac{\lambda_{\text{eff, nb}}}{\lambda_{\text{eff, I}}} \right)^{\beta} + F_{\text{Ly}\alpha} \quad (14)$$

$$\Delta\lambda'_{\text{V}} f_{\lambda, \text{V}} = f_{\lambda, \text{I}} \Delta\lambda'_{\text{V}} Q_{\text{V}} \left(\frac{\lambda_{\text{eff, V}}}{\lambda_{\text{eff, I}}} \right)^{\beta} + F_{\text{Ly}\alpha}. \quad (15)$$

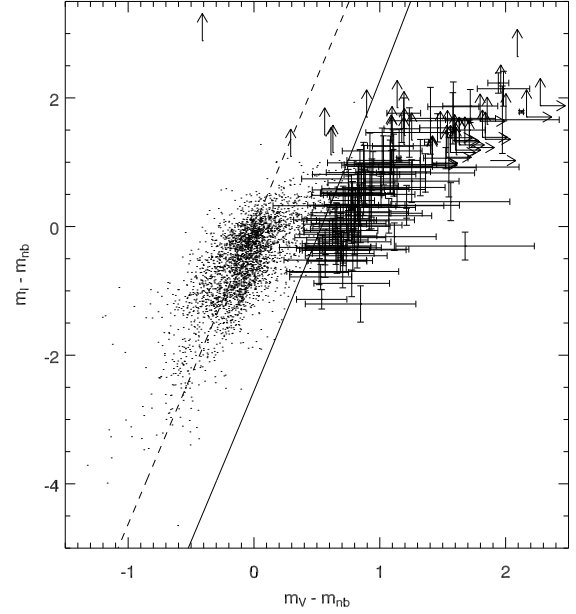


Fig. 3. Color-color diagram for the 3209 objects detected in the narrow-band image with a signal-to-noise greater than 5. The dashed line shows the color of objects with a rest-frame equivalent width of $EW_0 = 0 \text{ \AA}$. The solid line indicates where $EW_0 = 15 \text{ \AA}$. Objects not detected in the V-band and/or in the I-band are plotted with an arrow.

Subtraction of Eq. (14) from Eq. (15) results in an equation of the form $a^{\beta} - b^{\beta} = \text{constant}$. This equation was solved numerically.

When β was computed, the UV continuum flux density C and the Ly α line flux $F_{\text{Ly}\alpha}$ were calculated using Eqs. (9) and (10):

$$C = \frac{\Delta\lambda'_{\text{V}} f_{\lambda, \text{V}} - \Delta\lambda'_{\text{nb}} f_{\lambda, \text{nb}}}{\Delta\lambda'_{\text{V}} Q_{\text{V}} \lambda_{\text{eff, V}}^{\beta} - \Delta\lambda'_{\text{nb}} Q_{\text{nb}} \lambda_{\text{eff, nb}}^{\beta}} \quad (16)$$

and

$$F_{\text{Ly}\alpha} = \frac{f_{\lambda, \text{nb}} / (Q_{\text{nb}} \lambda_{\text{eff, nb}}^{\beta}) - f_{\lambda, \text{V}} / (Q_{\text{V}} \lambda_{\text{eff, V}}^{\beta})}{1 / (\Delta\lambda'_{\text{nb}} Q_{\text{nb}} \lambda_{\text{eff, nb}}^{\beta}) - 1 / (\Delta\lambda'_{\text{V}} Q_{\text{V}} \lambda_{\text{eff, V}}^{\beta})}. \quad (17)$$

With C and $F_{\text{Ly}\alpha}$, the equivalent width (EW) for each object was computed:

$$EW_{\text{obs}} = \frac{F_{\text{Ly}\alpha}}{C(\lambda_{\text{Ly}\alpha}(1+z))^{\beta}} \quad (18)$$

with $\lambda_{\text{Ly}\alpha}$ the wavelength of the Ly α line. The rest frame equivalent width (EW_0) is given by: $EW_0 = EW_{\text{obs}} / (1+z)$.

To estimate the uncertainties in the computed parameters, the observed flux densities were randomly varied 50 000 times over a range having a standard deviation equal to the uncertainty. The distributions of β , C , $F_{\text{Ly}\alpha}$ and EW_0 were used to estimate the errors in these quantities. Because the values of the equivalent width were not normally-distributed (Gaussian) around the central value, two errors were calculated, labelled

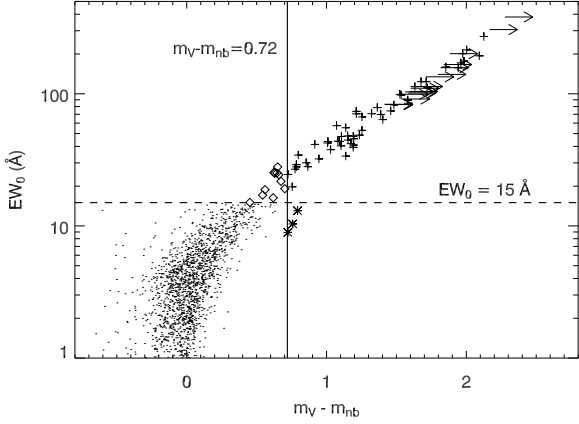


Fig. 4. Equivalent width (calculated from Eqs. 9–18) versus $m_V - m_{nb}$ color. For clarification, only objects with an $EW_0 > 1 \text{ \AA}$ are plotted and the error bars are left out. The solid line indicates a color of $m_V - m_{nb} = 0.72$, while the dashed line denotes the division between low ($EW_0 < 15 \text{ \AA}$) and high ($EW_0 > 15 \text{ \AA}$) equivalent width objects.

ΔEW_0^- and ΔEW_0^+ . These were computed from the values in the distribution that were outside the central 99.73% of all values. The difference between these values and the central value was taken as defining three sigma uncertainties.

For each object detected in the narrow-band image, the line flux, UV continuum and equivalent width and their errors were computed. Because no *I*-band data had been taken yet at the time that the candidates for the spectroscopy had to be selected, a flat spectrum ($\beta = -2$) was assumed for all sources. In Fig. 3, the $m_I - m_{nb}$ color is plotted against the $m_V - m_{nb}$ color. Following Venemans et al. (2002), objects with $EW_0 > 15 \text{ \AA}$ and $EW_0/\Delta EW_0^- > 3$ were selected as candidate Ly α emitters. Each individual Ly α candidate was inspected visually in order to remove spurious candidates, like leftover cosmic rays or objects in the “spikes” of bright stars. This resulted in a list of 77 candidate Ly α emitters with $EW_0 > 15 \text{ \AA}$ of which 6 had $15 \text{ \AA} < EW_0 < 20 \text{ \AA}$.

The main difference between the usage of Eq. (8) and Eqs. (9)–(18) to compute the equivalent width can be seen in Fig. 4. Using Eq. (8) (and thereby assuming a fixed slope of $\beta = -2$) the line with $EW_0 = 15 \text{ \AA}$ would lie at a constant $m_V - m_{nb} = 0.72$ (the solid line in Fig. 4). As a result, the EW_0 of three very blue objects (with $\beta < -2$) would be overpredicted, falsely selecting objects as Ly α emitters (e.g. the three crosses in Fig. 4). On the other hand, 11 red Ly α emitters with $\beta > -2$ would not pass the selection criterion $m_V - m_{nb} > 0.72$, while their EW_0 as calculated with Eqs. (9)–(18) is greater than 15 \AA (diamonds in Fig. 4).

4. Spectroscopy

4.1. Spectroscopic observations

Spectra of candidate Ly α emitters were taken during three separate observing sessions (see Table 1 for an overview). The first

spectroscopy session was carried out on 2001, September 22 with VLT/FORS2 in the multi-object spectroscopy mode with 19 movable slits of a fixed length of $\sim 20 - 22''$. The night was photometric, but because of strong winds ($> 12 \text{ m s}^{-1}$) the seeing fluctuated between $1''$ and $2''$. Spectra of 12 candidate Ly α emitters were obtained for $4 \times 2700 \text{ s}$ and $1 \times 1800 \text{ s}$ through $1''$ slits with the 1400V grism at a dispersion of $0.5 \text{ \AA pixel}^{-1}$. This grism was chosen for a number of reasons. First, it has a high peak efficiency of $\sim 85\%$ at wavelengths that corresponds to the redshifted Ly α line of the radio galaxy. Secondly, because observations of high redshift Ly α emitting galaxies have shown that the width of the Ly α line lies predominantly in the range $200 - 500 \text{ km s}^{-1}$ (e.g. Pentericci et al., 2000a; Dawson et al., 2002; Hu et al., 2004), the resolution of the grism ($R = 2100$, corresponding to $\sim 150 \text{ km s}^{-1}$) ensured that the Ly α emission line is marginally resolved (see Sect. 5.1), maximizing the signal-to-noise of the observed line. Also, the resolution is large enough to distinguish a high redshift Ly α emitting galaxy from a low redshift contaminant, the [O II] $\lambda\lambda 3726, 3729$ emitter. With the 1400V grism the [O II] doublet is resolved (see Fig. 5 for two examples). For the wavelength calibration exposures of He, HgCd and Ne arc lamps were obtained. The spectrophotometric standard star LTT 1788 (Stone & Baldwin, 1983; Baldwin & Stone, 1984) was observed with a $5''$ slit for the flux calibration.

On 2001, October 18, 19 and 20 spectra were obtained with FORS2 in the mask multi-object spectroscopy mode. In this mode objects are observed through a user defined, laser-cut mask with slits which had variable lengths (typically $10 - 12''$) and widths of $1''$. The nights were photometric with an average seeing of $1''$. The 1400V grism was used to observe 37 candidate Ly α emitters in two masks, of which 25 were included in both masks. The first mask was observed for $4 \times 2700 \text{ s}$ and the second mask for $10 \times 2700 \text{ s}$ and $1 \times 2100 \text{ s}$. The pixels were binned by 2×2 to avoid the noise in the spectra being dominated by read noise. This resulted in a dispersion of 1 \AA pixel^{-1} and a spatial scale of $0'.4 \text{ pixel}^{-1}$. Spectra of the standard star LTT 1788 were obtained for the flux calibration.

During the last observing session (2001, November 15 and 16), the instrument used was FORS1 on Melipal (VLT UT3). The main goal of this run was to measure the polarization of the radio galaxy (C. De Breuck et al., in preparation). Due to constraints on the positioning and orientation of the mask, only three candidate Ly α emitters could be observed. The width of the slits was $1''$. The total exposure time was 19800 s . The average seeing of these photometric nights was $0'.8$. The grism used for the observations was the “300V” with a resolution of 440, a dispersion of $2.64 \text{ \AA pixel}^{-1}$ and a spatial scale of $0'.2 \text{ pixel}^{-1}$. The spectrophotometric standard stars Feige 110 and LTT 377 (Stone & Baldwin, 1983; Baldwin & Stone, 1984) were observed for the flux calibration.

4.2. Data reduction

The spectra were reduced in the following way. Individual frames were flat-fielded using lamp flats, cosmic rays were identified and removed and the background was subtracted.

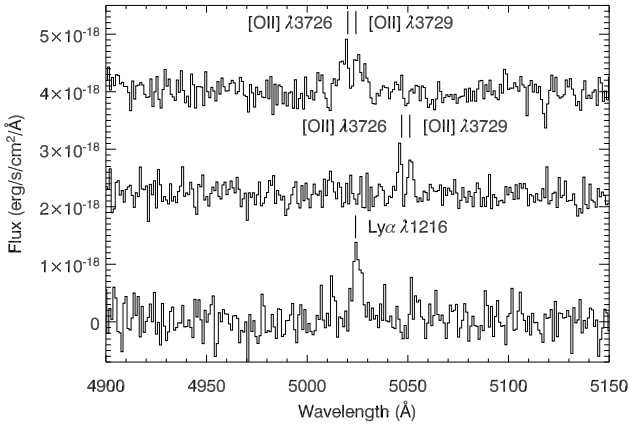


Fig. 5. Spectra of two [O II] emitters observed in the field (top two spectra). For comparison, the spectrum of one of the confirmed Ly α emitters is shown at the bottom. The spectra are offset from each other by $1.5 \times 10^{-18} \text{ erg s}^{-1} \text{ cm}^{-2} \text{ \AA}^{-1}$.

The next step was the extraction of the one-dimensional (1D) spectra. Typical aperture sizes were $1''$ – $1''.5$. If the spectrum of the object could be seen in the individual frames, then a spectrum was extracted from each frame and these spectra were combined. If the object was undetected in the individual frames, then the background subtracted two-dimensional frames were combined and a 1D spectrum was extracted from this image. All 1D spectra were wavelength calibrated using the arc lamp spectra. For spectra taken with the 1400V grism the rms of the wavelength calibration was always better than 0.05 \AA , which translates to $\Delta z = 0.00004$ at $z \sim 3.13$. The wavelength calibration with the 300V grism had an rms of 0.8 \AA ($\Delta z = 0.0007$ at $z \sim 3.13$). A heliocentric correction was applied on measured redshifts to correct for the radial velocity of the Earth in the direction of the observations. Finally, the spectra were flux calibrated. The fluxes of the photometric standard stars in the individual images were consistent with each other to within 5%, so we estimate that the flux calibration of the spectra is accurate to $\sim 5\%$.

4.3. Results

Spectra were obtained for a total of 40 candidate Ly α emitters, of which 11 were observed during two separate observing sessions, and the central radio galaxy. Of the 40 candidate emitters, only 7 failed to show an emission line. Six of these unconfirmed emitters had predicted line fluxes below $10^{-17} \text{ erg s}^{-1} \text{ cm}^{-2}$ and were probably too faint to be detected. Two of the 33 emission line objects showed two lines with almost equal strength, separated by $\sim 4 \text{ \AA}$ (Fig. 5). These objects were identified to be [O II] $\lambda\lambda 3726, 3729$ emitters at a redshift of ~ 0.35 . One of the [O II] emitters was re-observed in November 2001 and a nearly flat continuum was revealed with no break around the emission line, confirming that the object could not be a Ly α emitter at $z \sim 3.13$. None of the other emitters had more than one emission line in the spectrum. This excluded

Table 3. Characteristics of the Voigt absorption profiles derived from the spectra. For each absorption profile, its centre relative to the peak of the emission line, width (b) and H I column density (N) is printed.

Object	Centre	b (km s $^{-1}$)	$\log N$ (cm $^{-2}$)
344	-80 ± 10	52 ± 11	14.4 ± 0.1
995	-150 ± 20	74 ± 59	16.0 ± 2.5
1147	-70 ± 20	101 ± 24	14.6 ± 0.1
1203	-90 ± 10	104 ± 11	14.9 ± 0.1
1518	80 ± 50	38 ± 16	13.8 ± 0.2
	-210 ± 60	155 ± 52	15.0 ± 0.2
1612	-150 ± 10	79 ± 16	14.4 ± 0.1
1710	-130 ± 20	80 ± 30	14.1 ± 0.2
1867	-60 ± 20	30 ± 16	13.1 ± 0.3
2487	250 ± 170	108 ± 14	14.6 ± 0.1
	-1150 ± 200	629 ± 93	16.0 ± 0.2
3101	-40 ± 110	193 ± 131	14.4 ± 0.4
	-240 ± 20	79 ± 38	14.3 ± 0.3
3388	-130 ± 10	59 ± 13	14.3 ± 0.1
HzRG	200 ± 10	151 ± 9	14.9 ± 0.1
	-270 ± 10	245 ± 25	14.9 ± 0.1
	-660 ± 10	144 ± 20	14.8 ± 0.1
	-970 ± 20	131 ± 27	14.2 ± 0.1

identification of the emission line with [O III] $\lambda 5007$, because then the confirming [O III] $\lambda 4959$ would have been visible. Furthermore, a number of emitters showed an asymmetric line profile (Figs. 15–20), a feature often seen in spectra of high redshift Ly α emitters (e.g. Ajiki et al., 2002; Dawson et al., 2002). Therefore, the 31 remaining emitters were identified with being Ly α emitters. The fraction of contaminants in our sample is $2/33 = 6.1\%$, similar to the fraction of low redshift interlopers of 6.5% in the study of Ly α emitters at $z \sim 3.09$ of Steidel et al. (2000).

5. Properties of the Ly α emitting galaxies

The one-dimensional Ly α emission lines were fitted by a Gaussian function and – if absorption was clearly present – in combination with Voigt absorption profiles. The best fit Gaussian was used to calculate the redshift, line flux and $FWHM$ of each emitter. In Table 2 the properties of the confirmed Ly α emitters are summarized. The IDs correspond to the object’s number in the SExtractor catalog. The rest-frame equivalent width EW_0 was taken from the imaging. The star formation rate (SFR) was calculated using the Ly α line flux derived from the images, and assuming Case B recombination and using the H α luminosity to SFR conversion from Madau et al. (1998, see Sect. 5.4).

5.1. Line profiles

As mentioned in the previous paragraph, emitters which clearly showed an emission line with an absorbed blue wing (see Figs. 15–20) were fitted by a Gaussian emission line with one or more Voigt absorption profiles. The characteristics of the absorption profiles are listed in Table 3. The other emitters were

Table 2. Position and properties of the Ly α emission line of the 31 confirmed Ly α emitters and the radio galaxy.

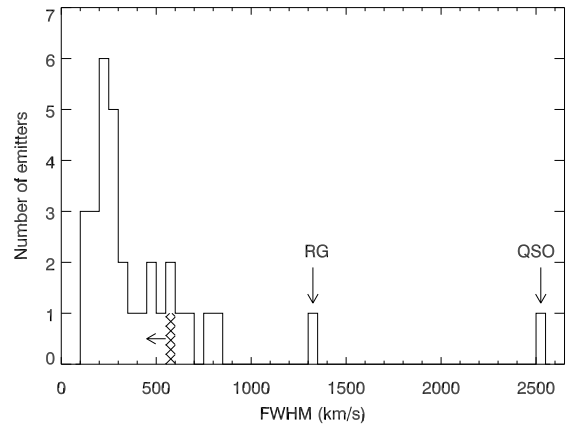
Object	Position		z	Flux 10^{-17} erg s $^{-1}$ cm $^{-2}$	EW_0 \AA	$FWHM$ km s $^{-1}$	$SFR_{Ly\alpha}$ M_{\odot} yr $^{-1}$
	α_{J2000}	δ_{J2000}					
344	03 18 05.83	-25 37 55.7	3.1332 \pm 0.0001	4.2 \pm 0.3	144 $^{+339}_{-30}$	260 \pm 20	2.8 \pm 0.2
695	03 18 13.26	-25 37 18.9	3.1712 \pm 0.0001	2.3 \pm 0.2	246 $^{+353}_{-51}$	180 \pm 20	4.0 \pm 0.4
748	03 18 21.51	-25 37 13.9	3.1359 \pm 0.0003	0.4 \pm 0.1	70 $^{+949}_{-20}$	260 \pm 50	1.1 \pm 0.2
995	03 18 09.67	-25 36 47.5	3.1239 \pm 0.0003	4.3 \pm 0.6	65 $^{+36}_{-14}$	450 \pm 30	2.6 \pm 0.4
1029	03 18 00.07	-25 36 43.6	3.1301 \pm 0.0007	0.3 \pm 0.1	39 $^{+17}_{-8}$	< 590	1.7 \pm 0.2
1099	03 18 02.79	-25 36 35.8	3.1313 \pm 0.0004	1.1 \pm 0.3	42 $^{+65}_{-11}$	240 \pm 70	1.4 \pm 0.3
1147	03 18 03.99	-25 36 31.9	3.1666 \pm 0.0003	6.0 \pm 2.2	318 $^{+1000}_{-90}$	290 \pm 40	1.4 \pm 0.2
1203	03 18 12.55	-25 36 23.0	3.1234 \pm 0.0002	10.3 \pm 1.8	78 $^{+24}_{-12}$	220 \pm 10	3.3 \pm 0.3
1361	03 18 01.57	-25 36 07.8	3.1306 \pm 0.0002	1.5 \pm 0.2	106 $^{+234}_{-24}$	210 \pm 40	2.6 \pm 0.3
1395	03 18 24.78	-25 36 05.7	3.1442 \pm 0.0011	1.8 \pm 0.6	< 30	790 \pm 190	0.4 \pm 0.1
1446	03 18 04.89	-25 35 57.7	3.1316 \pm 0.0002	0.5 \pm 0.1	12 $^{+8}_{-4}$	210 \pm 50	0.6 \pm 0.2
1498	03 18 14.14	-25 35 54.3	3.1319 \pm 0.0003	1.0 \pm 0.1	58 $^{+435}_{-18}$	460 \pm 60	0.6 \pm 0.1
1518	03 18 16.78	-25 35 46.2	3.1311 \pm 0.0007	3.2 \pm 0.8	23 $^{+2}_{-2}$	570 \pm 70	4.8 \pm 0.2
1612	03 18 03.49	-25 35 39.2	3.1222 \pm 0.0003	3.1 \pm 0.3	> 370	500 \pm 40	1.8 \pm 0.3
1710	03 18 15.17	-25 35 28.9	3.1462 \pm 0.0004	1.9 \pm 0.3	61 $^{+61}_{-14}$	420 \pm 50	1.0 \pm 0.1
1724	03 18 06.92	-25 35 26.2	3.1426 \pm 0.0002	0.4 \pm 0.1	> 150	160 \pm 50	0.9 \pm 0.1
1753	03 18 01.22	-25 35 22.3	3.1301 \pm 0.0001	1.5 \pm 0.2	32 $^{+16}_{-7}$	130 \pm 40	2.1 \pm 0.4
1759	03 18 25 50	-25 35 20.4	3.1271 \pm 0.0002	0.6 \pm 0.1	48 $^{+29}_{-11}$	120 \pm 50	2.5 \pm 0.4
1829	03 18 15.12	-25 35 13.1	3.1313 \pm 0.0002	0.7 \pm 0.1	24 $^{+19}_{-7}$	200 \pm 40	1.3 \pm 0.3
1867	03 18 09.00	-25 34 59.6	3.1358 \pm 0.0002	5.8 \pm 0.4	56 $^{+3}_{-3}$	650 \pm 40	11.6 \pm 0.2
1891	03 18 04.29	-25 35 04.9	3.1454 \pm 0.0002	0.6 \pm 0.1	< 31	130 \pm 40	0.8 \pm 0.2
1946	03 18 20.29	-25 34 59.4	3.1335 \pm 0.0003	0.7 \pm 0.1	< 19	260 \pm 50	0.7 \pm 0.3
1955	03 18 07.58	-25 34 55.5	3.1391 \pm 0.0003	0.7 \pm 0.1	> 139	330 \pm 60	1.1 \pm 0.2
1962	03 18 12.03	-25 34 52.8	3.1407 \pm 0.0007	1.7 \pm 0.4	33 $^{+12}_{-6}$	600 \pm 130	0.9 \pm 0.1
1968	03 18 05.14	-25 34 51.2	3.1564 \pm 0.0004	0.4 \pm 0.1	< 66	300 \pm 80	1.7 \pm 0.3
2413	03 18 20.40	-25 33 00.3	3.1339 \pm 0.0002	0.7 \pm 0.2	62 $^{+28}_{-11}$	200 \pm 50	2.7 \pm 0.3
2487	03 17 59.63	-25 34 01.3	3.1175 \pm 0.0024	19.3 \pm 2.6	202 $^{+9}_{-8}$	2510 \pm 190	^a
2637	03 18 22.52	-25 34 10.1	3.1224 \pm 0.0002	1.3 \pm 0.3	79 $^{+43}_{-16}$	200 \pm 50	3.2 \pm 0.5
2871	03 18 25.71	-25 33 40.5	3.1334 \pm 0.0003	0.4 \pm 0.1	> 75	250 \pm 70	0.7 \pm 0.1
3101	03 18 24.09	-25 32 12.2	3.1313 \pm 0.0003	4.3 \pm 1.2	114 $^{+47}_{-18}$	800 \pm 100	5.2 \pm 0.3
3388	03 18 26.09	-25 32 53.1	3.1379 \pm 0.0002	2.1 \pm 0.1	112 $^{+26}_{-13}$	370 \pm 20	8.6 \pm 0.3
H _z RG	03 18 12.01	-25 35 10.8	3.1307 \pm 0.0001	155.1 \pm 4.2	257 $^{+9}_{-8}$	1320 \pm 10	76.1 \pm 0.4 ^a

^a Object contains an AGN, therefore the estimated SFR is unreliable.

fitted by a single Gaussian. The observed width of the line was deconvolved with the instrumental width, which was 150 km s $^{-1}$ (see Sect. 4.1).

The radio galaxy has an emission line that can be fitted by a Gaussian with a $FWHM$ of \sim 1300 km s $^{-1}$. The line width is very similar to that of other H_zRGs (e.g. De Breuck et al., 2001; Willott et al., 2002). Only one of the confirmed emitters has a broad Ly α line. Emitter #2487 has a line $FWHM$ of \sim 2500 km s $^{-1}$, and is therefore likely to also harbour an AGN. The $FWHM$ of the Ly α emission line of the rest of the emitters ranges from 120 km s $^{-1}$ to 800 km s $^{-1}$ (Fig. 6), with a median of 260 km s $^{-1}$ and a mean of 340 km s $^{-1}$.

The inferred column densities of the absorbers are in the range of 10^{13} – 10^{16} cm $^{-2}$ (see Sect. 6). Using the spatial extent in the 2D spectra as an estimate of the size of the H I absorber, the amount of projected neutral H I near the emitters is in the range of $> 2 \times 10^2$ – $5 \times 10^4 M_{\odot}$ (see Sect. 6 for the details of the individual emitters). For the fainter Ly α emitters, it cannot be excluded that the troughs are due to substructure in the Ly α emitting regions, rather than H I absorption.

**Fig. 6.** Histogram of the line widths of the emitters.

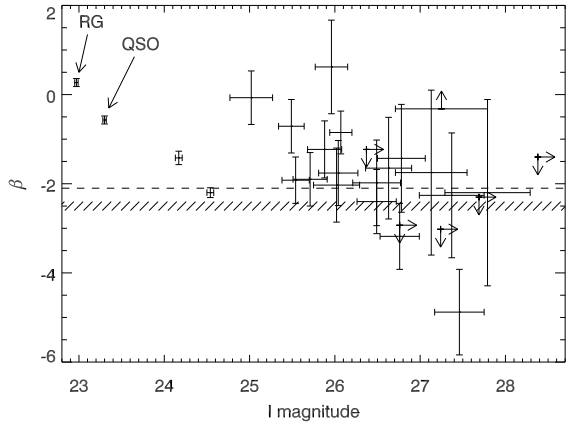


Fig. 7. I magnitude versus UV continuum slope β . The dashed line corresponds to $\beta = -2.1$, the color of an unobscured continuously star forming galaxy with an age of $\sim 10^8 - 10^9$ yr. The hashed area indicates the color of a young ($\sim 10^6$ yr), star forming galaxy.

5.2. Continuum colors

In Table 4, the magnitudes and UV continuum slopes of the confirmed emitters are listed (for a description on how the slope was calculated, see Sect. 3.3). For objects detected in the ACS image which were not resolved into several components, the I_{814} magnitude and the continuum slope β_{ACS} calculated using this magnitude is given. In Fig. 7 the I magnitude is plotted against the continuum slope. Excluding the radio galaxy and emitter #2487, which contains an AGN (Sect. 5.1), the UV continuum slope of the confirmed emitters ranges from $\beta = 0.62$ to $\beta = -4.88$ with a median of $\beta = -1.76$.

The blue median color of the Ly α emitters may be due to a selection effect. The candidate emitters for spectroscopy were selected when only one broad-band flux was available and a slope of $\beta = -2$ was assumed for all objects to compute the equivalent width (see Sect. 3.3 and Fig. 4). Because the narrow-band is on the blue side of the broad-band filter that was used, the equivalent width and line flux of bluer objects with $\beta < -2$ tend to have been overestimated, while “red” objects ($\beta > -2$) have an equivalent width and Ly α flux that are likely to be underestimated (see Sect. 3.3). This effect could have biased the spectroscopic sample towards blue objects. For example, the emitter with the bluest color, #1446, has an equivalent width of $EW_0 = 12 \text{ \AA}$, which falls below the selection criteria ($EW_0 > 15 \text{ \AA}$), but the object was selected for spectroscopy because it had $m_V - m_{\text{nb}} > 0.72$ (see discussion at the end of Sect. 3.3). To determine the effect of this bias, the color of a flux limited sample was determined. There are 31 (candidate) Ly α emitting objects with a Ly α flux $> 1.5 \times 10^{-17} \text{ erg s}^{-1} \text{ cm}^{-2}$ in the field, of which 25 are confirmed. Again excluding the radio galaxy and the AGN, the median color of the remaining 29 emitters is $\beta = -1.70$. This is bluer than the average color of Ly α emitting Lyman Break Galaxies (LBGs), which have a slope of $\beta = -1.09 \pm 0.05$ (Shapley et al., 2003).

Models of galaxies with active star formation predict UV continuum slopes in the range $\beta = -2.6$ to $\beta = -2.1$ for an unobscured, continuously star forming galaxy with ages between a few Myr and more than a Gyr (Leitherer et al., 1999). 18 out of the 27 (67%) confirmed Ly α emitters for which β could be measured, have colors within 1σ consistent with being an unobscured starburst galaxy. Of those, 15 (56% of the sample) have such blue colors with 1σ that they could be star forming galaxies with ages of order 10^6 yr, which have $\beta \sim -2.5$.

5.3. Morphologies

Of the 32 confirmed Ly α emitting sources, 19 (including the radio galaxy) were located in the area that was imaged by the ACS (Fig. 14). Two of these emitters remained undetected to a depth of $I_{814} > 27.1 \text{ mag arcsec}^{-2}$ (3σ). On the position of the radio galaxy, the ACS image shows several objects within $3''$ ($\sim 25 \text{ kpc}$), surrounded by low surface brightness emission ($\gtrsim 24.8 \text{ mag arcsec}^{-2}$, see Fig. 8). Such a clumpy structure is often seen at the position of HzRGs (e.g. Pentericci et al., 1999). Interestingly, there are three other Ly α emitters with morphologies that resemble the radio galaxy (Fig. 8). Each of these three objects consists of at least three clumps of emission, which are less than one kpc separated from each other. The remainder of the confirmed emitters can be identified with single objects in the ACS image.

To quantify the size of these objects, the half light radius (r_h) of each emitter was measured using the program SExtractor. The half light radius is defined as the radius of a circular aperture in which the flux is 50% of the total flux. However, as already discussed in Sect. 3.2 and shown in Fig. 2, the fraction of the total flux of an object that is missed by SExtractor increases when the object is fainter. As a consequence, the half light radius that is measured by SExtractor would underestimate the size of the object. To determine how much the half light radius was underestimated, galaxies with a range of sizes were varied in brightness and added to the ACS image, and the half light radii of those objects was measured by SExtractor. It was found, as mentioned above, that the fainter the object, the smaller its measured r_h , an effect that was stronger for larger galaxies, see Fig. 11. Using the results of these simulations, an attempt could be made to correct the measured sizes of the confirmed Ly α emitters. Unfortunately, this correction could overestimate the true size of compact objects (i.e. objects with a half light radius similar to that of stars). However, this only strengthens our conclusions (see below). In Table 5 the sizes of the emitters in the I_{814} -band are printed. The half light radii of the emitters range from $0''.06$ to $0''.18$. The error in the half light radius is defined as the half light radius divided by the signal-to-noise of the object. Translating the sizes directly to physical sizes, the measured half light radii correspond to 0.5 – 1.5 kpc . The median size is $\sim 1 \text{ kpc}$.

The mean half light radius of isolated, unsaturated stars in the field was found to be $\sim 0''.06$. Four of the emitters in the ACS field have a r_h that is within 1σ equal to the half light radii of the stars in the field. These four emitters are classified as unresolved (Fig. 9).

Table 4. Narrow-band, V , I and ACS I_{814} magnitudes and UV continuum slopes β of the confirmed emitters. Colors were measured in a circular aperture, while elliptical apertures were used to determine the total magnitudes (see Sect. 3.2). For objects with a signal-to-noise less than two a 2σ upper limit is given.

Object	NB magnitude	V magnitude	I magnitude	I_{814} magnitude	β	β_{ACS}
344	24.63 \pm 0.06	26.62 \pm 0.22	26.78 \pm 0.28	27.76 \pm 0.23	-1.43 \pm 1.21	-3.91 \pm 1.06
695	24.89 \pm 0.09	26.42 \pm 0.20	25.96 \pm 0.19	26.53 \pm 0.10	0.62 \pm 1.05	-0.92 \pm 1.09
748	25.45 \pm 0.14	27.03 \pm 0.37	27.13 \pm 0.42	–	-1.75 \pm 1.85	–
995	24.97 \pm 0.08	26.14 \pm 0.16	26.49 \pm 0.23	26.59 \pm 0.11	-2.40 \pm 0.72	-2.65 \pm 0.63
1029	25.00 \pm 0.07	26.19 \pm 0.12	26.76 \pm 0.23	–	-3.18 \pm 0.74	–
1099	25.23 \pm 0.13	26.39 \pm 0.28	26.49 \pm 0.28	–	-1.98 \pm 0.96	–
1147	25.74 \pm 0.12	27.83 \pm 0.44	> 28.38	– ^b	< -1.40	–
1203	24.79 \pm 0.06	26.00 \pm 0.11	– ^a	27.30 \pm 0.15	–	-4.77 \pm 0.55
1361	24.76 \pm 0.10	26.47 \pm 0.24	26.63 \pm 0.27	–	-1.65 \pm 1.14	–
1395	26.40 \pm 0.21	27.50 \pm 0.47	> 27.69	–	< -2.30	–
1446	25.53 \pm 0.10	26.32 \pm 0.12	27.46 \pm 0.29	26.55 \pm 0.12	-4.88 \pm 0.96	-2.46 \pm 0.46
1498	26.14 \pm 0.14	27.55 \pm 0.29	27.79 \pm 0.50	27.12 \pm 0.18	-2.20 \pm 2.09	-0.49 \pm 1.06
1518	23.65 \pm 0.02	24.47 \pm 0.03	24.54 \pm 0.04	24.57 \pm 0.03	-2.20 \pm 0.11	-2.12 \pm 0.12
1612	25.79 \pm 0.16	27.65 \pm 0.54	> 27.38	27.84 \pm 0.28	–	> -0.65
1710	25.51 \pm 0.08	27.09 \pm 0.19	27.37 \pm 0.38	27.34 \pm 0.19	-2.26 \pm 1.40	-2.18 \pm 0.78
1724	25.74 \pm 0.15	> 27.91	> 27.44	– ^b	–	–
1753	24.72 \pm 0.09	25.67 \pm 0.18	25.71 \pm 0.20	– ^c	-1.90 \pm 0.60	–
1759	24.77 \pm 0.09	25.87 \pm 0.19	26.02 \pm 0.27	–	-2.03 \pm 0.83	–
1829	25.11 \pm 0.13	25.73 \pm 0.26	25.02 \pm 0.25	– ^c	-0.07 \pm 0.60	–
1867	22.86 \pm 0.01	24.25 \pm 0.03	24.17 \pm 0.04	– ^c	-1.42 \pm 0.15	–
1891	25.56 \pm 0.13	26.76 \pm 0.29	> 27.24	27.45 \pm 0.20	< -3.02	-3.50 \pm 1.01
1946	25.58 \pm 0.18	26.40 \pm 0.36	> 26.76	–	< -2.93	–
1955	25.59 \pm 0.13	27.56 \pm 0.47	27.25 \pm 0.54	27.50 \pm 0.18	> -0.32	> -1.03
1962	25.44 \pm 0.08	26.44 \pm 0.11	26.07 \pm 0.13	26.10 \pm 0.08	-0.85 \pm 0.48	-0.99 \pm 0.38
1968	25.00 \pm 0.14	26.48 \pm 0.45	> 26.37	26.61 \pm 0.12	< -1.23	-1.89 \pm 1.63
2413	24.51 \pm 0.07	25.97 \pm 0.16	26.04 \pm 0.23	–	-1.76 \pm 0.73	–
2487	22.25 \pm 0.01	23.40 \pm 0.02	23.30 \pm 0.02	–	-0.57 \pm 0.09	–
2637	24.88 \pm 0.09	25.97 \pm 0.17	25.88 \pm 0.20	–	-1.23 \pm 0.64	–
2871	26.04 \pm 0.18	> 27.64	> 27.22	–	–	–
3101	23.99 \pm 0.04	25.70 \pm 0.12	25.49 \pm 0.15	–	-0.71 \pm 0.60	–
3388	23.31 \pm 0.03	25.25 \pm 0.09	25.54 \pm 0.16	–	-1.92 \pm 0.52	–
H _z RG	21.19 ^d \pm 0.01	23.31 ^d \pm 0.02	22.97 ^d \pm 0.02	– ^c	0.27 \pm 0.09	–

^a Photometry unreliable due to nearby bright star.

^b Undetected in the ACS image, $I_{814} > 27.1$ mag arcsec⁻²

^c Resolved by *HST* into several components.

^d Photometry influenced by nearby objects.

The sizes of the confirmed Ly α emitters can be compared to other high redshift galaxies, e.g. LBGs. Recently, sizes were measured of galaxies at various redshifts in the Great Observatories Origins Deep Survey (GOODS, Ferguson et al., 2004). For their analysis, they used SExtractor with circular apertures having a radius that is 10 times larger than the first radial moment of the light distribution to ensure that all the flux was inside the aperture. The survey was restricted to rest-frame luminosities between $0.7 L^*$ and $5 L^*$. Using the luminosity function of LBGs derived by Steidel et al. (1999), this corresponds to a magnitude range of $22.78 < m_R < 24.92$. Only two confirmed emitters located in the ACS field (#1518 and #1867) satisfy the luminosity criterion used in the GOODS analysis. Emitter #1867 is resolved into several clumps of emission. The size of emitter #1518 measured with the same input parameter as Ferguson et al. (2004), is $0''.106 \pm 0''.006$, consistent with

the $0''.102 \pm 0''.003$ derived using our own input parameters. The half light radius of emitter #1518 is among the smallest Ferguson et al. are finding. The average size of LBGs at $z \sim 3$ is $0''.28$ (~ 2.3 kpc). Thus, the Ly α emitters are small compared to LBGs at the same redshift, provided that the method we used to measure the sizes of the Ly α emitting galaxies gives comparable half light radii as the approach of Ferguson et al. (as was the case for emitter # 1518).

5.4. Star formation rate

The average star formation rate (SFR) of the confirmed emitters, as derived from the Ly α flux (see Table 2), is $2.5 M_{\odot} \text{ yr}^{-1}$ (excluding the radio galaxy and the QSO, emitter #2487). This calculation assumed a Ly α /H α ratio of 8.7 (Case B recombination, Brocklehurst, 1971) and a H α luminosity to SFR

Table 5. Half light radii of the confirmed emitters located within the field of the ACS.

Object	r_h (")	r_h (kpc)	s/n
344	0'07 \pm 0'03	< 0.8	4.8
695	0'10 \pm 0'02	0.6 \pm 0.2	10.5
995	0'09 \pm 0'01	0.5 \pm 0.2	10.2
1203	0'06 \pm 0'01	< 0.6	7.1
1446	0'14 \pm 0'02	1.0 \pm 0.2	9.4
1498	0'18 \pm 0'06	1.4 \pm 0.5	6.0
1518	0'10 \pm 0'01	0.7 \pm 0.1	43.1
1612	0'14 \pm 0'05	1.0 \pm 0.5	3.8
1710	0'10 \pm 0'03	0.6 \pm 0.4	5.8
1753	Clumpy	–	\sim 12
1829	Clumpy	–	\sim 7
1867	Clumpy	–	\sim 20
1891	0'10 \pm 0'03	< 1.3	5.5
1955	0'08 \pm 0'03	< 1.0	6.1
1962	0'13 \pm 0'01	1.0 \pm 0.1	12.8
1968	0'14 \pm 0'02	1.1 \pm 0.2	9.0
HzRG	Clumpy	–	\sim 35

conversion for a Salpeter initial mass function (IMF) from Madau et al. (1998):

$$SFR_{H\alpha} = \frac{L_{H\alpha}}{1.6 \times 10^{41} \text{ erg s}^{-1}}. \quad (19)$$

Because of Ly α absorption (see e.g. Fig. 15–20), this SFR calculation gives a lower limit.

An alternative way to estimate the SFR is to use the level of the UV continuum. The flux density at a wavelength of $\lambda_{\text{rest}} = 1500 \text{ \AA}$ can be converted to a SFR following the relation

$$SFR_{\text{UV}} = \frac{L_{\text{UV}}(\lambda_{\text{rest}} = 1500 \text{ \AA})}{8.0 \times 10^{27} \text{ erg s}^{-1} \text{ Hz}^{-1}} \quad (20)$$

for a Salpeter IMF (Madau et al., 1998). In Fig. 12 the SFR as calculated from the Ly α emission is plotted against the UV continuum SFR. On average, the two methods to calculate the SFR give the same result, with the SFR measured from the UV continuum a factor 1–1.5 higher than the Ly α inferred SFR. The average SFR of the emitters as measured by the UV continuum is $\lesssim 3.8 M_{\odot} \text{ yr}^{-1}$. This is much lower than the average SFR of LBGs, which is somewhere between 10 and 100 $M_{\odot} \text{ yr}^{-1}$ (e.g. Giavalisco, 2002).

Recent measurements of the polarization of the UV continuum of the radio galaxy indicate that the UV continuum is dominated by emission from stars. The contribution from a scattered AGN is small, which is implied by the upper limit on the polarization of the continuum of $P < 4\%$ (C. De Breuck et al., in preparation). If all the light at a rest-frame wavelength of 1500 \AA is due to young stars, then the SFR of the radio galaxy is $40.5 \pm 0.8 M_{\odot} \text{ yr}^{-1}$. No correction is made for dust absorption. This is similar to the uncorrected SFR (as calculated from the rest-frame UV continuum) in radio galaxies at $z \sim 2.5$ (e.g. Vernet et al., 2001) and a factor of ~ 5 lower than the SFR of the radio galaxy 4C41.17 at $z = 3.8$ (Chambers et al., 1990; Dey et al., 1997).

6. Notes on individual objects

- **#344:** The spectrum of this emitter is shown in Fig. 15. The Ly α line can be fitted by a combination of a Gaussian and a Voigt absorption profile which is located $80 \pm 10 \text{ km s}^{-1}$ blueward of the peak of the Gaussian. The fit is shown as the solid line in Fig. 15. From the 2D spectrum a lower limit of $2''$ ($\sim 16 \text{ kpc}$) on the linear size of the absorber could be derived, giving a lower limit on the H I mass of $M(\text{H I}) > 550 M_{\odot}$.
- **#995:** The spectrum of this object can be fitted by a Gaussian with a narrow Voigt profile centred $150 \pm 20 \text{ km s}^{-1}$ blueward of the emission peak (solid line in Fig. 15). The column density of the absorbing neutral hydrogen is nearly unconstrained by our spectrum and lies in the range $N(\text{H I}) \sim 10^{13.5-18.5}$. The absorber has a size of $> 2''$ in the 2D spectrum and taking a column density of 10^{16} cm^{-2} , the inferred mass of neutral hydrogen is at least $2 \times 10^4 M_{\odot}$.
- **#1147:** This object is one of the two emitters that were not detected in the ACS image down to a 3 sigma magnitude limit of 27.1 mag arcsec $^{-2}$. Its redshift is $\sim 2400 \text{ km s}^{-1}$ redder than the median redshift of the emitters, and is therefore unlikely to be associated with the protocluster (see Sect. 7.2). The spectrum shows absorption which is located $70 \pm 20 \text{ km s}^{-1}$ blueward of the peak of the unabsorbed emission (Fig. 16). A lower limit of $550 M_{\odot}$ can be given for the H I mass.
- **#1203:** This emitter is unresolved in both the VLT and ACS images (Fig. 9). The spectrum is shown in Fig. 16. The absorption is located $90 \pm 10 \text{ km s}^{-1}$ to the blue of the peak of the Gaussian. We obtain a lower limit for the mass of neutral hydrogen responsible for the absorption of $> 1700 M_{\odot}$.
- **#1446:** The emitter has a very blue continuum slope ($\beta = -4.88 \pm 0.96$). The computed equivalent width of $EW_0 = 12 \text{ \AA}$ is below the selection criterion ($EW_0 > 15 \text{ \AA}$). The VLT I -band magnitude and the I_{814} magnitude derived from the ACS image are different at the 2.8σ level, taking the differences in effective wavelength of the filters into account. Using the ACS magnitude the continuum slope becomes -2.61 and the $EW_0 \sim 20 \text{ \AA}$. The object is resolved in the ACS image and has a half light radius of $1.0 \pm 0.2 \text{ kpc}$ (Fig. 10).
- **#1498:** In the ACS image, an object with $r_h = 1.4 \pm 0.5 \text{ kpc}$ is located $\sim 0.5''$ from the position of the weak emitter in the VLT image.
- **#1518:** This is the fourth brightest Ly α emitter in the field. The object is extended in both the Ly α image and the ACS image (see Sect. 5.3 and Fig. 10). The emission line can be fitted by a Gaussian with two Voigt profiles superimposed, one $80 \pm 50 \text{ km s}^{-1}$ to the red and the other $210 \pm 60 \text{ km s}^{-1}$ to the blue of the Gaussian (Fig. 17). This results in a lower limit of the mass of H I of $2300 M_{\odot}$.
- **#1612:** This emitter has a faint continuum ($I_{814} = 27.84 \pm 0.28$) and is barely detected in ACS image (signal-to-noise of ~ 4), and is marginally resolved (Table 5, Fig. 10). The spectrum shows absorption of $10^{14.4 \pm 0.1} \text{ cm}^{-2}$ H I, located

- 150 \pm 10 km s $^{-1}$ to the blue of the redshift of this galaxy (Fig. 17).
- #1710: This is a blue emitter ($\beta = -2.26 \pm 1.40$) with an absorption trough on the blue wing of the emission line (see Fig. 18), the result of at least 200 M_{\odot} of H I.
 - #1753: At the position of this Ly α emitter, the ACS image shows three separate objects located within ~ 8 kpc (Fig. 8).
 - #1829: This object is resolved by the ACS into an elongated structure consisting of several objects (Fig. 8).
 - #1867: Denoted as galaxy “A” by LF96, a spectrum of this object taken under bad seeing conditions confirms the redshift measured by LF96 (Table 2). The Ly α line is asymmetric and can be fitted by a Gaussian and one Voigt absorber, which is 60 \pm 20 km s $^{-1}$ blueward of the Ly α peak (Fig. 18). The VLT narrow-band image shows an extended Ly α halo of ~ 25 kpc (Fig. 8), while in ACS image the object is very clumpy.
 - #1968: This emitter was undetected in the VLT *I*-band, but in the ACS image an object with a half light radius of 1.1 \pm 0.2 kpc is visible.
 - #2487: This emitter has the brightest Ly α line in the field after the radio galaxy, and is called galaxy “B” in LF96. As mentioned in Sect. 5.1, the Ly α line is broad ($FWHM \sim 2500$ km s $^{-1}$) which is most likely caused by an AGN. The spectrum is characterized by a large absorption trough with a column density of $N(\text{H I}) \sim 10^{14.6}$ cm $^{-2}$. Furthermore, the red wing of the Ly α line is much broader than the blue wing. The spectrum can be fitted with two absorbers, located 250 \pm 170 km s $^{-1}$ to the red and 1150 \pm 200 km s $^{-1}$ to the blue of the centre of the emission line. The inferred mass of H I is $> 5 \times 10^4 M_{\odot}$.
 - #2719: This is galaxy “C” from LF96. Galaxy “C” was not selected as a candidate Ly α emitter in our images. It has colors comparable to those quoted in LF96, but an EW_0 of $1.0_{-1.1}^{+1.2}$. LF96 measured an $EW_0 > 12$ Å and a line flux of $\sim 5 \times 10^{-17}$ erg s $^{-1}$ cm $^{-2}$, although no spectrum was taken of this object to confirm the existence of the line. An explanation for the fact that this galaxy is not selected by us as an emission line candidate could be that the large width of the narrow-band filter used by LF96, making it sensitive to a wider redshift range than our filter. Their filter was sensitive to Ly α emitters having redshifts in the range $z = 3.08 - 3.16$, while our filter is sensitive to the redshift range $z = 3.12 - 3.17$. Galaxy “C” could be a Ly α emitter with a redshift between $z = 3.08$ and $z = 3.12$, and it would therefore be part of the protocluster, but not be included as one of our candidates (see Sect. 7.2).
 - #3101: The Ly α line of this emitter is broad (800 \pm 100 km s $^{-1}$ $FWHM$, see Fig. 19), as compared to the median line width of the emitters (260 km s $^{-1}$). The spectrum can be fitted by a Gaussian, superimposed by two Voigt absorbers located 40 \pm 110 and 240 \pm 20 km s $^{-1}$ to the blue of the emission, the result of at least $\sim 1000 M_{\odot}$ of H I.
 - #3388: This blue Ly α emitter ($\beta = -1.92 \pm 0.52$) shows an absorption trough 130 \pm 10 km s $^{-1}$ blueward of the emission redshift (Fig. 20), implying a neutral Hydrogen mass of $> 625 M_{\odot}$.

- **Radio galaxy MRC 0316–257**: The absorption structure of the radio galaxy is complicated. Only a Gaussian emission line profile with 4 separate absorbers gives a reasonable fit (solid line in Fig. 20 and Table 3). The absorbers are 200 \pm 10 km s $^{-1}$ to the red of the peak of the Gaussian and 270 \pm 10 km s $^{-1}$, 660 \pm 10 km s $^{-1}$ and 970 \pm 20 km s $^{-1}$ to the blue. Approximately 2'' to the north-east of the radio galaxy is a foreground galaxy, with a clear spiral structure in the ACS image. An emission line was detected in a spectrum of this object, with a wavelength around 6965 Å, most likely [O II] at $z \sim 0.87$ (C. De Breuck, private communications).

7. A protocluster at $z = 3.13$?

7.1. Volume density

Several surveys have been carried out to estimate the (field) volume density of Ly α emitters at $z \sim 3$ (e.g. Cowie & Hu, 1998; Hu et al., 1998; Kudritzki et al., 2000; Ciardullo et al., 2002; Fynbo et al., 2003). To estimate the (over)density of Ly α emitters in our field, we will compare our numbers with those found in the survey of Ciardullo et al. (2002), since it covers the largest area of all the surveys, and of Fynbo et al. (2003), because they present the deepest and spectroscopically most complete comparison sample of blank field $z \sim 3$ Ly α emitters.

Ciardullo et al. (2002) made a blank field survey to estimate the density of emission line sources and to calculate the contamination of intra-cluster planetary nebulae searches. They searched for faint emission line sources in a 0.13 deg 2 field at a wavelength of 5019 Å. They found 21 objects with an observed equivalent width greater than 82 Å and a $m_{\text{nb}} < 24.3$. Assuming all their sources are Ly α emitters at $z \sim 3.13$, the volume density of field emitters is $n_{\text{field}} = 2.4_{-0.5}^{+0.6} \times 10^{-4}$ Mpc $^{-3}$. Applying the same selection criteria to our data, 5 emission line objects (excluding the radio galaxy) are found in the field around 0316–257, all confirmed to be Ly α emitters at $z \sim 3.13$. This gives a density of $n_{0316} = 5.4_{-2.3}^{+3.7} \times 10^{-4}$ Mpc $^{-3}$. The density in the 0316 field is therefore a factor $2.2_{-1.0}^{+1.8}$ higher than the field density. The large errors on this number are due to small number statistics.

More recently, Fynbo et al. (2003) presented the first results of a program to detect faint Ly α emitters at $z \sim 3$. They used the same VLT narrow-band filter as described in Sect. 2.1 to image a field that contained a damped Ly α absorber. The 5σ detection limit for point sources in their narrow-band image is $m_{\text{nb}} < 26.5$ as measured in a circular aperture with a size twice the seeing $FWHM$, is very similar to our 5σ detection limit ($m_{\text{nb}} < 26.4$). They found 27 candidate Ly α emitters with an equivalent width greater than 12.5–25 Å, the limit depending on the predicted line flux. Subsequent spectroscopy confirmed that 18 of the 22 candidate emitters observed are Ly α emitters and two were foreground [O II] emitters. Assuming that the seven unconfirmed candidate emitters are all Ly α emitters at $z \sim 3$, the number of Ly α emitters down to a flux limit of 6×10^{-18} erg s $^{-1}$ cm $^{-2}$ in their field is 25. Our number of emitters selected with the same equivalent width limits is ~ 75 after correction for foreground contaminants. This implies a density of $3.0_{-0.7}^{+0.9}$ times the field density. Roughly, we find three times

the number of Ly α emitters as might be expected from field surveys.

Maier et al. (2003) gathered measured abundances of Ly α emitters from the literature, shifted them to $z = 3.5$ and fitted a model function through the points (a description of the model can be found in Thommes & Meisenheimer, 2004). They predict approximately 2325 Ly α emitters per deg² in a volume with $\Delta z = 0.1$ with line fluxes exceeding 5×10^{-18} erg s⁻¹ cm⁻². If their model is correct, then ~ 15 Ly α emitting galaxies at $z = 3.13$ are expected within our volume brighter than 7×10^{-18} erg s⁻¹ cm⁻². Applying this limit, we find 63 galaxies or 59 galaxies if we correct for possible foreground contaminants. Of these, 29 are spectroscopically confirmed. The density is a factor $4.0_{-0.5}^{+0.6}$ higher than the model prediction, in agreement with the above estimates.

To summarize, the density of Ly α emitters near the radio galaxy is a factor 2–4 higher than the field density, indicating that the radio galaxy might reside in an overdense region.

7.2. Velocity distribution

The velocity distribution of the emitters is plotted in Fig. 13. The response of the narrow-band filter used to select the candidate emitters for spectroscopy is also shown. Interestingly, the emitters are not distributed homogeneously over the filter, but most of them appear to cluster on the blue side of the filter. The emitters which show absorption in their emission line profiles seem to be distributed more homogeneously, but this could be due to the small number of objects.

To test whether the clustering of emitters in redshift space is significant, Monte Carlo simulations of the redshift distribution were performed. 10000 realizations with 31 emitters were reproduced, with the narrow-band filter curve as the redshift probability function for each emitter. The mean of the observed redshift distribution ($z = 3.136$) differs 2.6σ compared to the simulated distribution ($z = 3.146 \pm 0.004$) and the width of the observed redshift distribution differs by 1.7σ (0.012 compared to 0.022 ± 0.006). In total, the measured redshift distribution deviates from the simulated one by 3.07σ . This means that a redshift distribution as observed was reproduced in only 0.2% of the cases. The peak of velocity distribution of the Ly α emitters lies within 200 km s^{-1} of the redshift of the radio galaxy (Fig. 13), providing evidence that most of the Ly α emitters are physically associated with the radio galaxy. Taking together, the observed overdensity of Ly α emitters in our field (Sect. 7.1), combined with the peak in the redshift distribution provide compelling evidence that the Ly α emitters reside in a protocluster at $z \sim 3.13$.

8. Properties of the protocluster

In this Section, we discuss the macro properties of the Ly α emitters in the protocluster.

8.1. Velocity dispersion

To determine the velocity dispersion of the emitters, the bi-weight scale estimator was used (Beers et al., 1990). This is

the most appropriate scale estimator for samples of 20–50 objects (Beers et al., 1990). The velocity dispersion is $640 \pm 195 \text{ km s}^{-1}$, corresponding to a *FWHM* of $1510 \pm 460 \text{ km s}^{-1}$. This is significantly smaller than the width of the narrow-band filter, which has a *FWHM* of $\sim 3500 \text{ km s}^{-1}$. Although most Ly α emitters are likely to be members of the protocluster, the three emitters with velocities $> 1500 \text{ km s}^{-1}$ from the peak of the distribution (Fig. 13) are probably field galaxies. Ignoring these three field galaxies, the velocity dispersion drops to $535 \pm 100 \text{ km s}^{-1}$. On the lower redshift side (negative velocities), no clear edge is visible in the distribution. This could be due to the decrease in sensitivity of the narrow-band filter on this side of the redshift distribution. If the protocluster extends to much lower redshifts, our estimate of the velocity dispersion is a lower limit.

8.2. Spatial distribution

The spatial distribution of the emitters is shown in Fig. 14, where the circles, diamonds and triangles represent the spectroscopically confirmed emitters, and with the sizes of the symbols scaled according to the velocity offset from the median of the emitters. The pluses are unconfirmed candidate Ly α emitters satisfying our selection criteria (see Sect. 3.3). The majority of these candidates (96%) has not yet been observed spectroscopically, while the remaining 4% were too faint to be confirmed. The imaging field of view ($3.3 \times 3.3 \text{ Mpc}^2$ at $z = 3.13$) is not large enough to show clear boundaries of the structure.

8.3. Mass

At a redshift of $z = 3.13$, the age of the Universe is only 2.2 Gyr. Taking the velocity dispersion as a typical velocity for a galaxy in the protocluster, it would take at least 5 Gyr to cross the structure, making it highly unlikely that the protocluster is near virialization. Therefore, the virial theorem cannot be used to calculate the mass of the protocluster.

Another way to compute the mass is to use the (comoving) volume V occupied by the overdensity, the (current) mean density of the Universe $\bar{\rho}$ and the mass overdensity of the protocluster δ_m :

$$M = \bar{\rho} V (1 + \delta_m) = \bar{\rho} V (1 + \delta_{\text{gal}}/b). \quad (21)$$

where b is the bias parameter ($b \equiv \delta_{\text{gal}}/\delta_m$), relating the observed galaxy overdensity ($\delta_{\text{gal}} = n_{0316}/n_{\text{field}} - 1$) to the mass overdensity and $\bar{\rho} = 3.5 \times 10^{10} M_{\odot} \text{ Mpc}^{-3}$ for the cosmological parameters used in this paper.

The weighted mean of the three density estimates in Sect. 7.1 is $n_{0316}/n_{\text{field}} = 3.3_{-0.4}^{+0.5}$, giving an overdensity of $\delta_{\text{gal}} = 2.3_{-0.4}^{+0.5}$. Taking $V = 9.3 \times 10^3 \text{ Mpc}^3$ (Sect. 2.2) and $b = 3 - 6$ (Steidel et al., 1998; Shimasaku et al., 2003) results in a mass for the protocluster within the observed volume of $4 - 6 \times 10^{14} M_{\odot}$. Because the size of the protocluster is unconstrained (e.g. Fig. 14), this mass estimate is a lower limit.

However, the redshift range of protocluster galaxies is likely to be smaller than the redshifts for which the narrow-band filter is sensitive (see Fig. 13). Assuming that the three

outlying galaxies on the red side of the filter as field galaxies, the redshift range of the protocluster galaxies is 0.029 and the volume occupied by these emitters is $5.4 \times 10^3 \text{ Mpc}^3$. This estimate of the volume does not take into account the redshift space distortions caused by peculiar velocities (Steidel et al., 1998, see below). Assuming that in total $\sim 10\%$ of the (candidate) emitters are field galaxies (see Sect. 7.2), the density of emitters within this volume with respect to the field density is $1 + \delta_{\text{gal}} = 3.3^{+0.5}_{-0.4} \times 0.9 \times \frac{9331}{5400} = 5.1^{+0.8}_{-0.6}$. In this approach, the relation between the mass overdensity δ_m and the observed galaxy overdensity δ_{gal} is (Steidel et al., 1998):

$$1 + b\delta_m = C(1 + \delta_{\text{gal}}), \quad (22)$$

where C takes into account the redshift space distortions (Steidel et al., 1998). Assuming that the structure is just breaking away from the Hubble flow, C can be approximated by

$$C = 1 + f - f(1 + \delta_m)^{1/3} \quad (23)$$

(Steidel et al., 1998), with f the rate of growth of perturbations at the redshift of the protocluster (Lahav et al., 1991). f not only depends on z , but also on Ω_M and Ω_Λ . In the cosmology adopted in this paper ($\Omega_M = 0.3$ and $\Omega_\Lambda = 0.7$), f is close to 1 at high redshift ($z > 2$, Lahav et al., 1991).

Again taking $b = 3 - 6$, the computed mass of the protocluster is $> 3 - 5 \times 10^{14} M_\odot$. As both the redshift range of the galaxies and the size of the protocluster could be larger than is observed (see Sects. 8.1 and 8.2), this estimate is again a lower limit. The computed mass roughly corresponds to the virial mass of the Virgo cluster (e.g. Fouqué et al., 2001).

9. Nature of the Ly α emitters

What can we deduce about the nature of the Ly α emitters in our field? Four of the 16 emitters (25%) detected in the ACS image are unresolved and may be narrow-line ($FWHM \lesssim 1000\text{--}2000 \text{ km s}^{-1}$, e.g. Bennert et al., 2002) QSOs. The number density of faint ($21 < m_R < 25.5$) QSOs near $z = 3$ in the LBG survey of Steidel and collaborators (Steidel et al., 2003) is 250 QSO deg^{-2} in a redshift interval $\Delta z \approx 0.6$ (Steidel et al., 2002). They observe a ratio of narrow-line to broad-line QSOs of $N(\text{narrow})/N(\text{broad}) = 1.2 \pm 0.4$ (Steidel et al., 2002). Assuming an overdensity of galaxies in our field of $n_{0316}/n_{\text{field}} = 4.0$ (Sect. 7.1), the predicted number of QSOs in field is ~ 1 . Indeed, one (broad-line) QSO is found (emitter #2487). Extrapolating the faint end of the QSO luminosity function given by Hunt et al. (2004) to $m_R > 25.5$, the number of QSOs near MRC 0316–257 with $25.5 < m_R < 28.5$ is calculated to be < 1 , making the identification of the Ly α emitters with QSO unlikely. Another reason against the classification of the Ly α emitters as QSOs is the continuum slope of narrow-line QSOs in the LBG survey of $\beta = -0.4$ (Steidel et al., 2002). This is much redder than the median of the unresolved emitters ($\beta \sim -1.43$). We therefore conclude that all the Ly α emitters are star forming galaxies³

³ We can not entirely exclude that some of the emitters harbour a (concealed) AGN. A 40 ks exposure by the *Chandra* X-ray observatory is scheduled for early 2005, which should help to estimate the fraction of the Ly α emitters that contains an AGN.

The next question is how the properties of the Ly α emitters compare to those of the LBG population as a whole.

- *Continuum luminosity:* Besides that of the radio galaxy and the broad-line QSO, the continuum of the emitters is faint, the brightest emitter having $m_R = 24.24$ (using $m_R = -2.5 \log(f_\nu(\lambda_{\text{rest}} = 1700\text{\AA})) - 48.59$) and the faintest $m_R > 28.45$. Using $m_* = 24.53$ at $z = 3.13$ (Steidel et al., 1999), this corresponds to luminosities ranging from $1.3 L^*$ to $< 0.03 L^*$. Roughly 90% of the emitters are fainter than $m_R = 25.5$, the spectroscopic limit for LBGs. A similar percentage was found by Fynbo et al. (2003).
- *Size:* A comparison of the sizes of Ly α emitters with those of LBGs at $z \sim 3$ suggests that Ly α emitters are generally smaller (with $r_h < 1.5 \text{ kpc}$) than LBGs which have an average size of $r_h \sim 2.3 \text{ kpc}$.
- *Color:* The colors of the confirmed emitters are, on average, very blue. The median UV continuum slope is $\beta = -1.76$, bluer than the average slope of LBGs with Ly α emission ($\beta \sim -1.09$; Shapley et al., 2003). A large fraction of the confirmed emitters ($\sim 2/3$) have colors consistent with negligible absorption and could be dust-free starburst galaxies.

Summarizing these properties, the Ly α emitters are on average fainter, bluer and smaller than $z \sim 3$ LBGs.

Various models have been proposed to explain the properties of Ly α emitters. Based on rest-frame optical photometry of LBGs, Shapley et al. (2001) concluded that LBGs with Ly α in emission are “old” (age $> \text{few} \times 10^8 \text{ yr}$), while “young” (age $< 10^8 \text{ yr}$) LBGs have Ly α in absorption. This could be explained by the young galaxies being dusty which caused the absorption of Ly α photons, while the older galaxies are more quiescent with less dust and superwinds which allow Ly α photons to escape. Other groups have suggested that strong Ly α emitters are young star forming galaxies which was derived from the blue colors and high equivalent widths of the Ly α emitters (e.g. LF96, Rhoads & Malhotra, 2001; Keel et al., 2002; Malhotra & Rhoads, 2002; Tapken et al., 2004). Trying to connect these observations, various authors (e.g. Friaça & Terlevich, 1999; Thommes & Meisenheimer, 2004) discuss a model in which a forming galaxy has two Ly α bright phases: an initial phase when the galaxy has started the very first period of star formation and is still nearly dust free. Due to supernova explosions, the interstellar medium will be enriched with metals, and dust will form in the galaxy. This dust will absorb the Ly α photons, extinguishing the Ly α emission line. A second Ly α bright phase occurs at a later time when strong galactic winds facilitate the escape of Ly α emission.

The observations of Ly α emitters in our field support this second picture, and the Ly α emitting galaxies might be young star forming galaxies in their first starburst phase. This should be confirmed by deep infrared observations. Modelling the spectral energy distribution of the Ly α emitters from the UV to the rest-frame optical should allow the discrimination of Ly α emitters being either young dust-free galaxies or more evolved star forming galaxies with an underlying old stellar population.

10. Implications of a protocluster at $z = 3.13$

10.1. Star formation rate density

The total UV star formation rate density (SFRD) of the confirmed emitters (excluding the radio galaxy) within the volume of the narrow-band filter is $\lesssim 0.0127 \pm 0.0003 M_{\odot} \text{ yr}^{-1} \text{ Mpc}^{-3}$. The SFRD derived from observations of LBGs at $z \sim 3$ with $m_R \lesssim 27$ is $0.0184 \pm 0.0034 M_{\odot} \text{ yr}^{-1} \text{ Mpc}^{-3}$ (Steidel et al., 1999). Using the same magnitude limit, we find a SFRD of $0.0109 \pm 0.0002 M_{\odot} \text{ yr}^{-1} \text{ Mpc}^{-3}$. This is a lower limit, because it does not include a contribution from the radio galaxy, the emitters with only a limit on their UV SFR are ignored and no correction has been made for incompleteness. Assuming that only 20–25% of the star forming, UV bright galaxies at $z \sim 3$ have a Ly α line satisfying our selection criteria (Steidel et al., 2000; Shapley et al., 2003), then the SFRD around MRC 0316–257 is roughly > 2.4 – 3.0 times higher than in the field, in agreement with the number density of the Ly α emitters.

It should be noted that the total SFRD in the protocluster might be much higher. From rest-frame UV and optical colors, Steidel et al. (1999) and Shapley et al. (2001) found that the UV continuum is on average attenuated by a factor of ~ 5 . Also, very dusty, obscured galaxies could be missing. For example, De Breuck et al. (2004) found an overdensity of bright sources at 1.2 mm wavelength in the field of the protocluster near the radio galaxy TN J1338–1942 at $z = 4.1$. These objects could contribute substantially to the total SFR within the protocluster.

10.2. Enrichment of the intracluster medium

It is interesting to estimate the metal production in the protocluster surrounding MRC 0316–257. At redshift $z \sim 0.3$, the intracluster medium (ICM) in clusters has a metallicity of 0.2 – $0.3 Z_{\odot}$ (e.g. Mushotzky & Loewenstein, 1997), showing little evolution up to $z \sim 1.2$ (Tozzi et al., 2003; Hashimoto et al., 2004; Maughan et al., 2004; Rosati et al., 2004).

The extinction corrected total star formation rate density of UV-bright star forming galaxies at $z \sim 3.1$ is $\sim 0.13 M_{\odot} \text{ yr}^{-1} \text{ Mpc}^{-3}$ (Steidel et al., 1999; Giavalisco et al., 2004). The protocluster has a volume of $5.4 \times 10^3 \text{ Mpc}^3$ and a galaxy overdensity of $n_{0316}/n_{\text{field}} = 5.1$ (Sect. 8.3). This gives a total SFR in the protocluster of $\sim 3580 M_{\odot} \text{ yr}^{-1}$, ignoring any contribution to the SFR from very dusty, obscured starforming galaxies. Taking an average yield of 0.02 (Lia et al., 2002), this means that $\sim 72 M_{\odot}$ of metals are produced every year. Taking $4 \times 10^{14} M_{\odot}$ as the mass of the protocluster (Sect. 8.3) and assuming a baryon fraction of $\Omega_b/\Omega_M = 0.17$ (e.g. Spergel et al., 2003) and assuming that the star formation rate in the protocluster is constant with time, then enough metals can be produced to enrich the baryons in the protocluster to $0.2 Z_{\odot}$ at $z \sim 1$. However, a large fraction ($> 90\%$) of the produced metals must escape the galaxies in which they are formed. A possible mechanism to inject the metals into the ICM are supernova-driven outflows (e.g. Heckman et al., 1995; Aguirre et al., 2001), which are frequently seen in $z \sim 3$ LBGs (e.g. Pettini et al., 2001; Adelberger et al., 2003). This simple

calculation shows that the star formation rate in the protocluster is high enough to enrich the ICM to the observed value at lower redshifts.

10.3. High redshift protoclusters associated with radio galaxies

Based on the high volume density of Ly α emitters near MRC 0316–257, which is a factor of $3.3^{+0.5}_{-0.4}$ higher as compared to blank fields, and the small velocity distribution of the confirmed emitters ($FWHM$ of 1510 km s^{-1}) compared to the width of the narrow-band filter ($FWHM \sim 3500 \text{ km s}^{-1}$), we conclude that the Ly α emitters are located in a protocluster of galaxies with an estimated mass of > 3 – $6 \times 10^{14} M_{\odot}$. A likely scenario is that this protocluster will evolve and form a massive cluster of galaxies. The radio galaxy at the centre of the protocluster has the properties expected of the progenitor of a massive cD elliptical. The clumpy appearance of the radio galaxy in the ACS image could be explained as a merger of smaller subunits, and is very similar to *HST* observations of other $z \sim 2$ – 3 radio galaxies (e.g. Pentericci et al., 1999).

Based on the observations obtained in our VLT large program, the protocluster around MRC 0316–257 is not unique. We have found galaxy overdensities around all five radio galaxies (with redshifts between $z = 2.16$ and $z = 4.1$) that were studied to a similar depth as the 0316 field (Kurk et al., 2000; Pentericci et al., 2000a; Venemans et al., 2002, 2003; Kurk et al., 2004). Each of these radio galaxy field has at least 20 confirmed protocluster members, the velocity dispersions of the protoclusters range from 300 km s^{-1} to 1000 km s^{-1} and the associated masses are $> 10^{14} M_{\odot}$ (Venemans et al., 2003). At an even higher redshift, $z = 5.2$, we found a similar overdensity of Ly α emitters near the radio galaxy TN J0924–2201 (Venemans et al., 2004). In a future paper, we will describe and compare the properties of these radio galaxy protoclusters (Venemans et al. in prep).

Acknowledgements. We are grateful to the staff of Paranal, Chile, for their excellent support. We thank Michiel Reuland, Rogier Windhorst and Andrew Zirm for useful discussions and the referee, Paul Francis, for helpful suggestions. GKM acknowledges funding by an Academy Professorship of the Royal Netherlands Academy of Arts and Sciences (KNAW). The work by WvB was performed under the auspices of the U.S. Department of Energy, National Nuclear Security Administration by the University of California, Lawrence Livermore National Laboratory under contract No. W-7405-Eng-48. The NRAO is operated by associated universities Inc, under cooperative agreement with the NSF. This work was supported by the European Community Research and Training Network “The Physics of the Intergalactic Medium”.

References

- Adelberger, K. L., Steidel, C. C., Shapley, A. E., & Pettini, M. 2003, *ApJ*, 584, 45
- Aguirre, A., Hernquist, L., Schaye, J., et al. 2001, *ApJ*, 561, 521
- Ajiki, M., Taniguchi, Y., Murayama, T., et al. 2002, *ApJ*, 576, L25

- Appenzeller, I. & Rupprecht, G. 1992, *The Messenger*, 67, 18
- Archibald, E. N., Dunlop, J. S., Hughes, D. H., et al. 2001, *MNRAS*, 323, 417
- Athreya, R. M., Kapahi, V. K., McCarthy, P. J., & van Breugel, W. J. M. 1998, *A&A*, 329, 809
- Baldwin, J. A. & Stone, R. P. S. 1984, *MNRAS*, 206, 241
- Baugh, C. M., Cole, S., Frenk, C. S., & Lacey, C. G. 1998, *ApJ*, 498, 504
- Beers, T. C., Flynn, K., & Gebhardt, K. 1990, *AJ*, 100, 32
- Bennert, N., Falcke, H., Schulz, H., Wilson, A. S., & Wills, B. J. 2002, *ApJ*, 574, L105
- Bertin, E. & Arnouts, S. 1996, *A&AS*, 117, 393
- Bessell, M. S. 1979, *PASP*, 91, 589
- Best, P. N. 2000, *MNRAS*, 317, 720
- Best, P. N., Lehnert, M. D., Miley, G. K., & Röttgering, H. J. A. 2003, *MNRAS*, 343, 1
- Blakeslee, J. P., Anderson, K. R., Meurer, G. R., Benítez, N., & Magee, D. 2003a, in *ASP Conf. Ser. 295: Astronomical Data Analysis Software and Systems XII*, 257
- Blakeslee, J. P., Franx, M., Postman, M., et al. 2003b, *ApJ*, 596, L143
- Brocklehurst, M. 1971, *MNRAS*, 153, 471
- Bunker, A. J., Warren, S. J., Hewett, P. C., & Clements, D. L. 1995, *MNRAS*, 273, 513
- Carilli, C. L., Röttgering, H. J. A., van Ojik, R., Miley, G. K., & van Breugel, W. J. M. 1997, *ApJS*, 109, 1
- Chambers, K. C., Miley, G. K., & van Breugel, W. J. M. 1990, *ApJ*, 363, 21
- Ciardullo, R., Feldmeier, J. J., Krelove, K., Jacoby, G. H., & Gronwall, C. 2002, *ApJ*, 566, 784
- Cowie, L. L. & Hu, E. M. 1998, *AJ*, 115, 1319
- Dawson, S., Spinrad, H., Stern, D., et al. 2002, *ApJ*, 570, 92
- De Breuck, C., Bertoldi, F., Carilli, C., et al. 2004, *A&A*, in press
- De Breuck, C., Neri, R., Morganti, R., et al. 2003a, *A&A*, 401, 911
- De Breuck, C., Neri, R., & Omont, A. 2003b, *New Astronomy Review*, 47, 285
- De Breuck, C., van Breugel, W. J. M., Röttgering, H., et al. 2001, *AJ*, 121, 1241
- De Breuck, C., van Breugel, W. J. M., Stanford, S. A., et al. 2002, *AJ*, 123, 637
- Della Ceca, R., Scaramella, R., Gioia, I. M., et al. 2000, *A&A*, 353, 498
- Deutsch, E. W. 1999, *AJ*, 118, 1882
- Dey, A., van Breugel, W. J. M., Vacca, W. D., & Antonucci, R. 1997, *ApJ*, 490, 698
- Ferguson, H. C., Dickinson, M., Giavalisco, M., et al. 2004, *ApJ*, 600, L107
- Ford, H. C., Bartko, F., Bely, P. Y., et al. 1998, in *Proc. SPIE Vol. 3356, Space Telescopes and Instruments V*, Pierre Y. Bely; James B. Breckinridge; Eds., 234
- Fouqué, P., Solanes, J. M., Sanchis, T., & Balkowski, C. 2001, *A&A*, 375, 770
- Friaga, A. C. S. & Terlevich, R. J. 1999, *MNRAS*, 305, 90
- Fruchter, A. S. & Hook, R. N. 2002, *PASP*, 114, 144
- Fynbo, J. P. U., Ledoux, C., Møller, P., Thomsen, B., & Burud, I. 2003, *A&A*, 407, 147
- Fynbo, J. P. U., Møller, P., Thomsen, B., et al. 2002, *A&A*, 388, 425
- Giavalisco, M. 2002, *ARA&A*, 40, 579
- Giavalisco, M., Dickinson, M., Ferguson, H. C., et al. 2004, *ApJ*, 600, L103
- Hashimoto, Y., Barcons, X., Böhringer, H., et al. 2004, *A&A*, 417, 819
- Heckman, T. M., Dahlem, M., Lehnert, M. D., et al. 1995, *ApJ*, 448, 98
- Hill, G. J. & Lilly, S. J. 1991, *ApJ*, 367, 1
- Hu, E. M., Cowie, L. L., Capak, P., et al. 2004, *AJ*, 127, 563
- Hu, E. M., Cowie, L. L., & McMahon, R. G. 1998, *ApJ*, 502, L99
- Hunt, M. P., Steidel, C. C., Adelberger, K. L., & Shapley, A. E. 2004, *ApJ*, 605, 625
- Jarvis, M. J., Rawlings, S., Eales, S., et al. 2001, *MNRAS*, 326, 1585
- Keel, W. C., Cohen, S. H., Windhorst, R. A., & Waddington, I. 1999, *AJ*, 118, 2547
- Keel, W. C., Wu, W., Waddington, I., Windhorst, R. A., & Pascarella, S. M. 2002, *AJ*, 123, 3041
- Kudritzki, R.-P., Méndez, R. H., Feldmeier, J. J., et al. 2000, *ApJ*, 536, 19
- Kurk, J. D., Pentericci, L., Röttgering, H. J. A., & Miley, G. K. 2004, *A&A*, in press
- Kurk, J. D., Röttgering, H. J. A., Pentericci, L., et al. 2000, *A&A*, 358, L1
- Lahav, O., Rees, M. J., Lilje, P. B., & Primack, J. R. 1991, *MNRAS*, 251, 128
- Landolt, A. U. 1992, *AJ*, 104, 340
- Large, M. I., Mills, B. Y., Little, A. G., Crawford, D. F., & Sutton, J. M. 1981, *MNRAS*, 194, 693
- Le Fèvre, O., Deltorn, J. M., Crampton, D., & Dickinson, M. 1996, *ApJ*, 471, L11
- Leitherer, C., Schaerer, D., Goldader, J. D., et al. 1999, *ApJS*, 123, 3
- Lia, C., Portinari, L., & Carraro, G. 2002, *MNRAS*, 330, 821
- Madau, P. 1995, *ApJ*, 441, 18
- Madau, P., Pozzetti, L., & Dickinson, M. 1998, *ApJ*, 498, 106
- Maier, C., Meisenheimer, K., Thommes, E., et al. 2003, *A&A*, 402, 79
- Malhotra, S. & Rhoads, J. E. 2002, *ApJ*, 565, L71
- Maughan, B. J., Jones, L. R., Ebeling, H., et al. 2003, *ApJ*, 587, 589
- Maughan, B. J., Jones, L. R., Ebeling, H., & Scharf, C. 2004, *MNRAS*, 351, 1193
- McCarthy, P. J., Kapahi, V. K., van Breugel, W. J. M., & Subrahmanya, C. R. 1990, *AJ*, 100, 1014
- Monet, D. B. A., Canzian, B., Dahn, C., et al. 1998, *VizieR Online Data Catalog*, 1252, 0
- Monet, D. G. 1998, *Bulletin of the American Astronomical Society*, 30, 1427
- Moorwood, A. F. 1997, in *Proc. SPIE Vol. 2871, p. 1146–1151, Optical Telescopes of Today and Tomorrow*, Arne L. Ardeberg; Ed., 1146–1151
- Mushotzky, R. F. & Loewenstein, M. 1997, *ApJ*, 481, L63
- Oke, J. B. 1974, *ApJS*, 27, 21
- Papadopoulos, P. P., Röttgering, H. J. A., van der Werf, P. P.,

- et al. 2000, *ApJ*, 528, 626
- Pascarelle, S. M., Windhorst, R. A., Driver, S. P., Ostrander, E. J., & Keel, W. C. 1996, *ApJ*, 456, L21
- Pentericci, L., Kurk, J. D., Carilli, C. L., et al. 2002, *A&A*, 396, 109
- Pentericci, L., Kurk, J. D., Röttgering, H. J. A., et al. 2000a, *A&A*, 361, L25
- Pentericci, L., Röttgering, H. J. A., Miley, G. K., et al. 1999, *A&A*, 341, 329
- Pentericci, L., Van Reeve, W., Carilli, C. L., Röttgering, H. J. A., & Miley, G. K. 2000b, *A&AS*, 145, 121
- Pettini, M., Shapley, A. E., Steidel, C. C., et al. 2001, *ApJ*, 554, 981
- Press, W. H., Rybicki, G. B., & Schneider, D. P. 1993, *ApJ*, 414, 64
- Reuland, M., Röttgering, H., van Breugel, W., & De Breuck, C. 2004, *MNRAS*, 353, 377
- Rhoads, J. E. & Malhotra, S. 2001, *ApJ*, 563, L5
- Rosati, P., Stanford, S. A., Eisenhardt, P. R., et al. 1999, *AJ*, 118, 76
- Rosati, P., Tozzi, P., Ettori, S., et al. 2004, *AJ*, 127, 230
- Röttgering, H. J. A., West, M. J., Miley, G. K., & Chambers, K. C. 1996, *A&A*, 307, 376
- Schlegel, D. J., Finkbeiner, D. P., & Davis, M. 1998, *ApJ*, 500, 525
- Shapley, A. E., Steidel, C. C., Adelberger, K. L., et al. 2001, *ApJ*, 562, 95
- Shapley, A. E., Steidel, C. C., Pettini, M., & Adelberger, K. L. 2003, *ApJ*, 588, 65
- Shimasaku, K., Ouchi, M., Okamura, S., et al. 2003, *ApJ*, 586, L111
- Spergel, D. N., Verde, L., Peiris, H. V., et al. 2003, *ApJS*, 148, 175
- Stanford, S. A., Holden, B., Rosati, P., et al. 2002, *AJ*, 123, 619
- Steidel, C. C., Adelberger, K. L., Dickinson, M., et al. 1998, *ApJ*, 492, 428
- Steidel, C. C., Adelberger, K. L., Giavalisco, M., Dickinson, M., & Pettini, M. 1999, *ApJ*, 519, 1
- Steidel, C. C., Adelberger, K. L., Shapley, A. E., et al. 2000, *ApJ*, 532, 170
- . 2003, *ApJ*, 592, 728
- Steidel, C. C., Hunt, M. P., Shapley, A. E., et al. 2002, *ApJ*, 576, 653
- Stevens, J. A., Ivison, R. J., Dunlop, J. S., et al. 2003, *Nature*, 425, 264
- Stone, R. P. S. & Baldwin, J. A. 1983, *MNRAS*, 204, 347
- Tapken, C., Appenzeller, I., Mehlert, D., Noll, S., & Richling, S. 2004, *A&A*, 416, L1
- Thommes, E. & Meisenheimer, K. 2004, *A&A*, accepted (astro-ph/0312363)
- Toft, S., Mainieri, V., Rosati, P., et al. 2004, *A&A*, 422, 29
- Tozzi, P., Rosati, P., Ettori, S., et al. 2003, *ApJ*, 593, 705
- Venemans, B. P., Kurk, J. D., Miley, G. K., et al. 2002, *ApJ*, 569, L11
- Venemans, B. P., Miley, G. K., Kurk, J. D., Röttgering, H. J. A., & Pentericci, L. 2003, *The Messenger*, 111, 36
- Venemans, B. P., Röttgering, H. J. A., Overzier, R. A., et al. 2004, *A&A*, 424, L17
- Vernet, J., Fosbury, R. A. E., Villar-Martín, M., et al. 2001, *A&A*, 366, 7
- White, S. D. M. & Rees, M. J. 1978, *MNRAS*, 183, 341
- Willott, C. J., Rawlings, S., Blundell, K. M., et al. 2002, *MNRAS*, 335, 1120
- Zirm, A. W., Dickinson, M., & Dey, A. 2003, *ApJ*, 585, 90

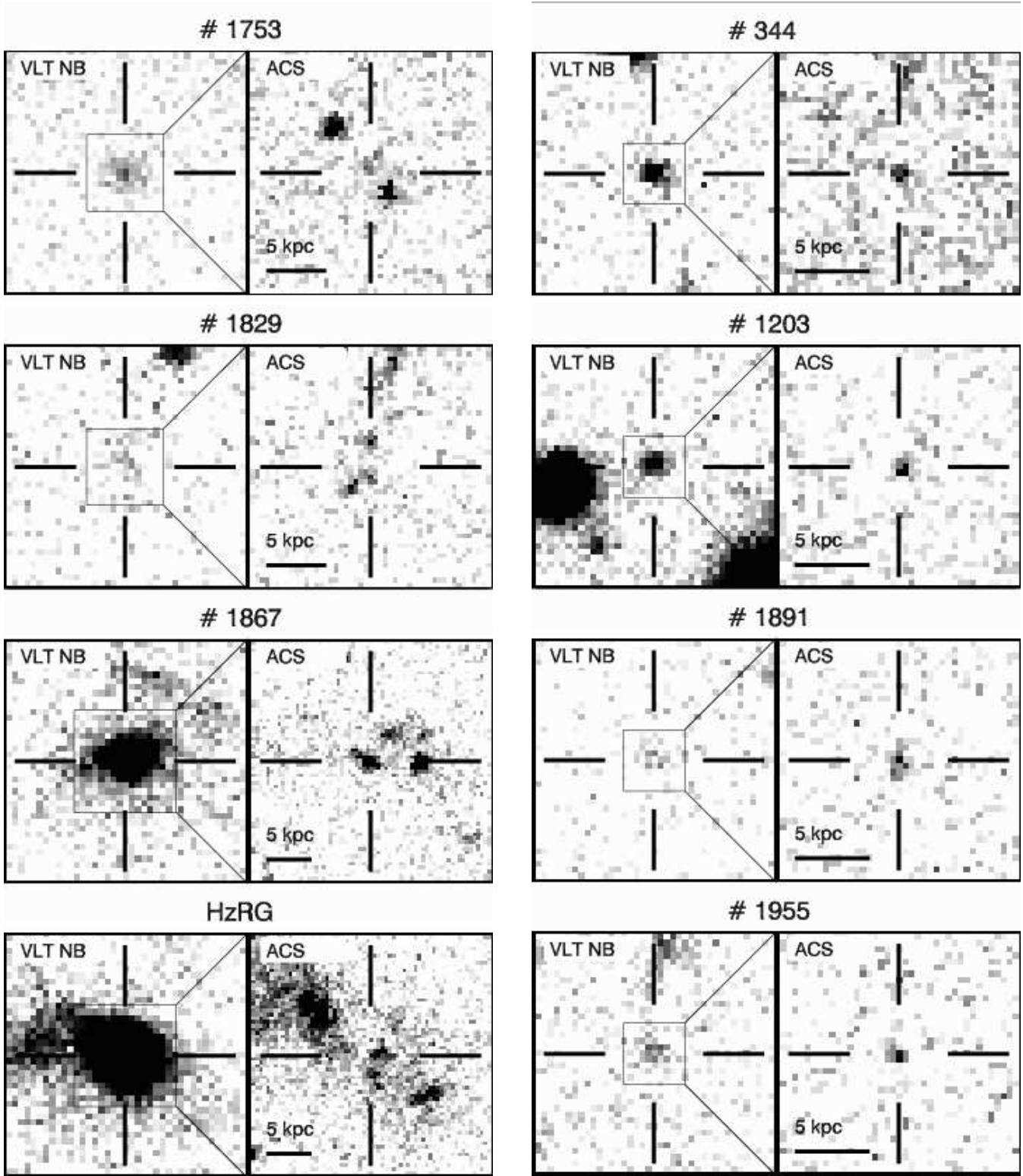


Fig. 8. VLT narrow-band and ACS images of Ly α emitters with a clumpy counterpart in the ACS image. The cutouts of the narrow-band image are $\sim 8''$ on the side. The ACS images are zoomed in on the centre of the narrow-band image. The grayscale ranges from 0.5 to 5 times the rms background noise. The emission to the left of the radio galaxy in the VLT image (and in the top-left corner of the ACS image) are from a foreground galaxy at $z \sim 0.87$ (see also Sect. 6).

Fig. 9. VLT narrow-band and ACS images of Ly α emitters that remained unresolved in the ACS image. The cutouts of the narrow-band image are $\sim 8''$ on the side. The grayscale ranges from 0.5 to 5 times the rms background noise.

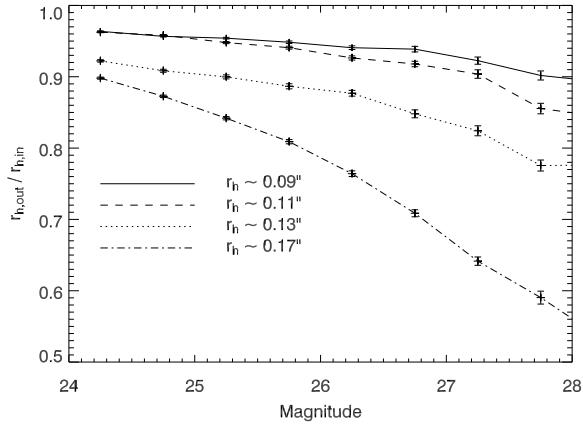


Fig. 11. The ratio of recovered size over input size as a function of magnitude in the ACS image. The fainter and/or larger the objects, the more the size is underestimated.

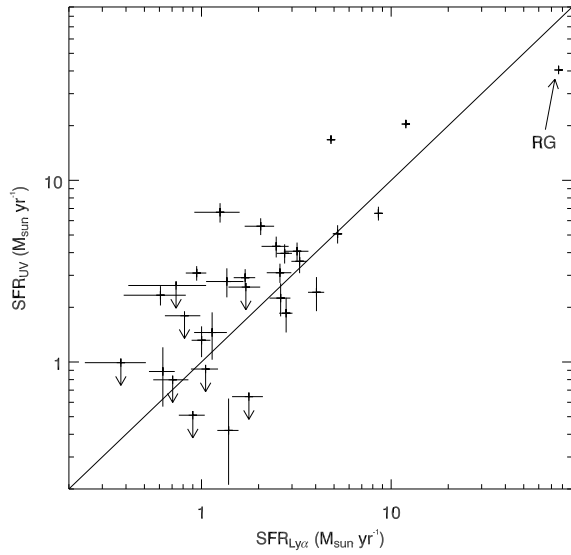


Fig. 12. SFR calculated from the UV continuum plotted against the SFR computed using the Ly α flux for the confirmed Ly α emitters.

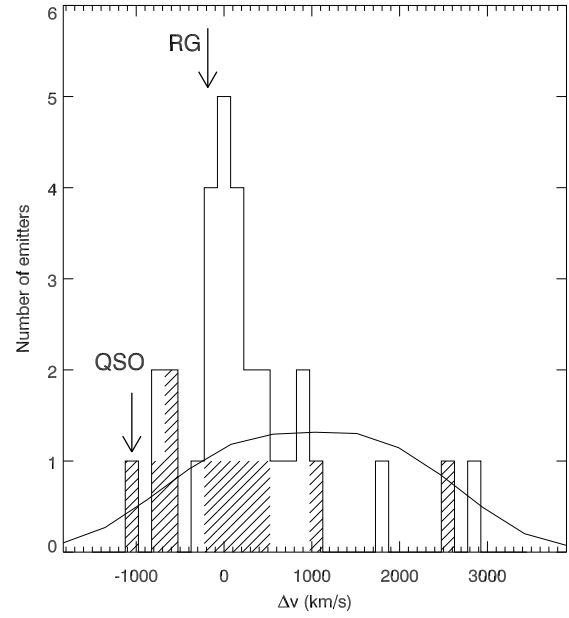


Fig. 13. Velocity distribution of the confirmed Ly α emitters. The bin size is 150 km s^{-1} . The median redshift of the confirmed emitters $z = 3.1313$ is taken as the zero-point. The velocities of the radio galaxy and the QSO are indicated with arrows. The solid line represents the selection function of the narrow-band filter, normalized to the total number of emitters found. The hashed histogram represents the velocities of emitters with absorption in their line profile. The three objects in the red part of the filter (with a velocity greater than 1500 km s^{-1}) might not be part of the protocluster.

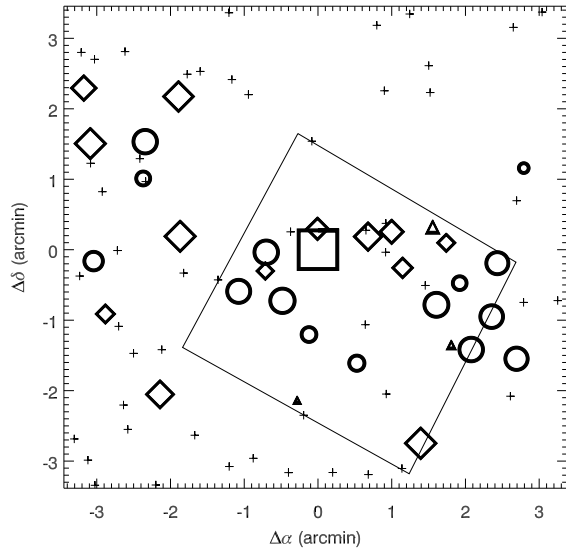


Fig. 14. Spatial distribution of Ly α emitters around the radio galaxy MRC 0316–257 (denoted by a square). The confirmed emitters in the protocluster are represented by circles (emitters with a redshift smaller than the median, $z < 3.1313$) and diamonds (emitters with $z > 3.1313$). The triangles show the position of the three Ly α emitting galaxies with a velocity > 1500 km s $^{-1}$ from the median velocity of the emitters. The sizes of the symbols are scaled according to the velocity offset from the median, with larger symbols representing emitters with a redshift closer to the median redshift. The pluses are objects satisfying the selection criteria (see Sect. 3.3), but are not (yet) confirmed. The quadrangle represents the outline of the ACS image.

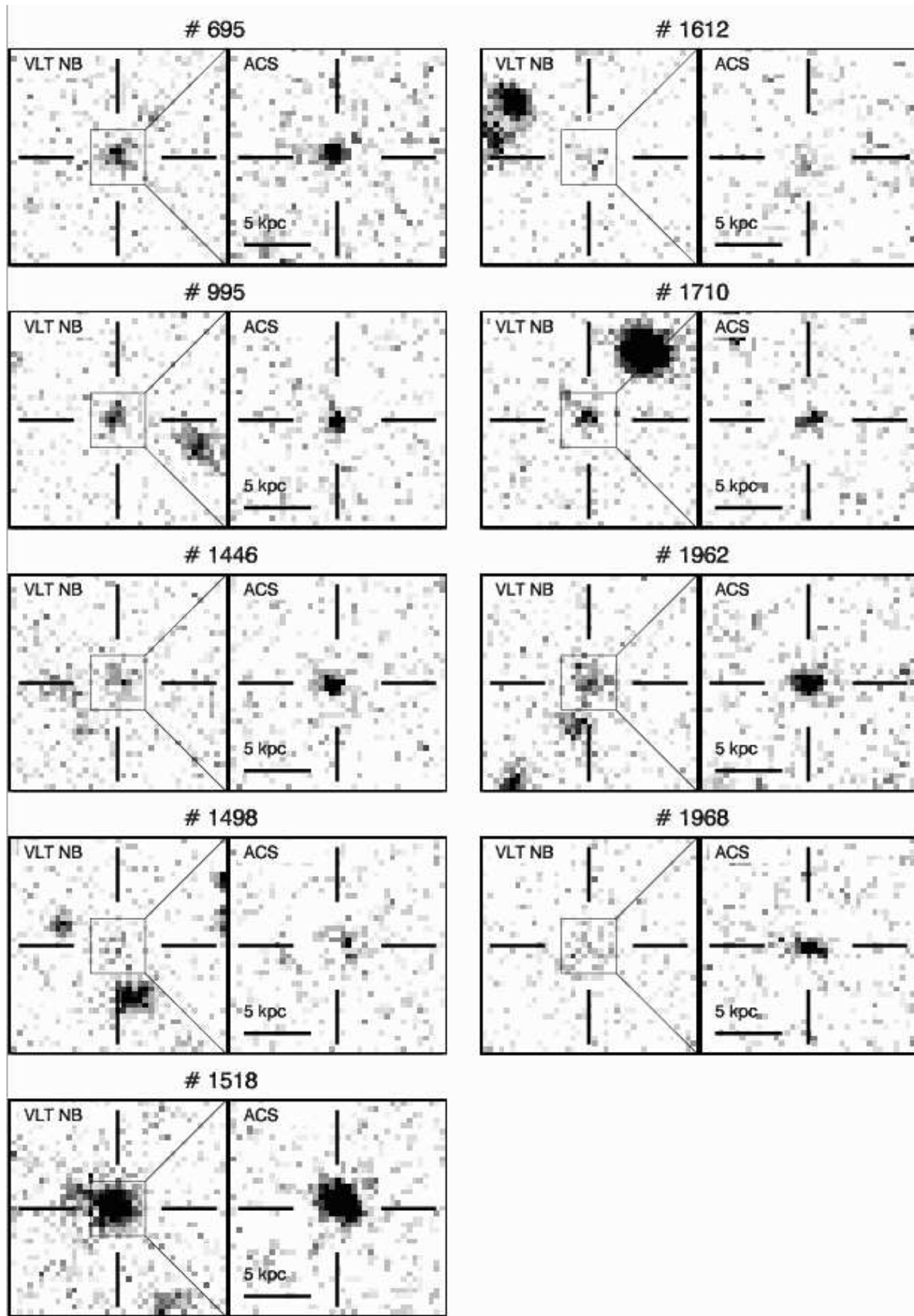


Fig. 10. VLT narrow-band and ACS images of Ly α emitters, which are resolved by the *HST*. The cutouts of the narrow-band image are $\sim 8''$ on the side. The grayscale ranges from 0.5 to 5 times the rms background noise.

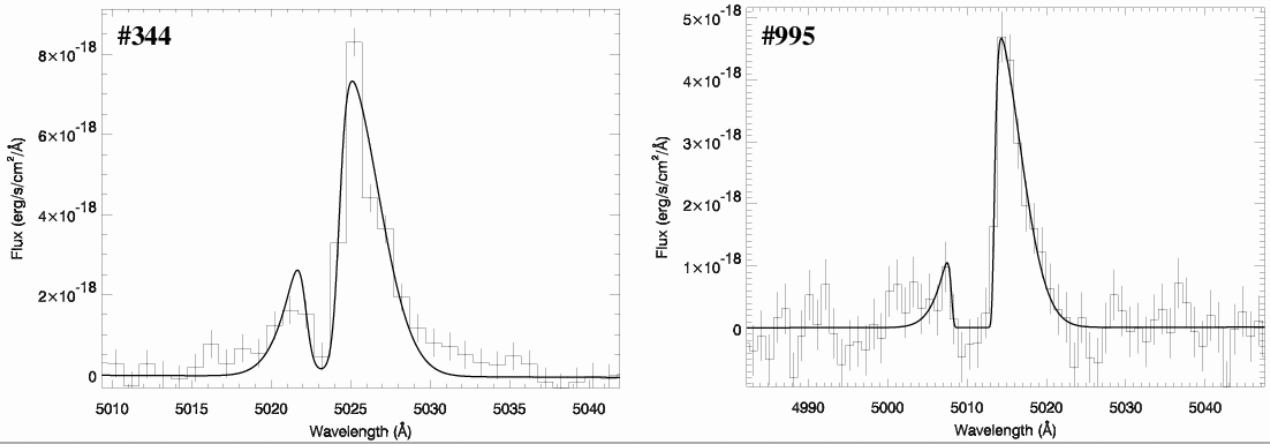


Fig. 15. Spectra of emitter #344 (left) and #995 (right).

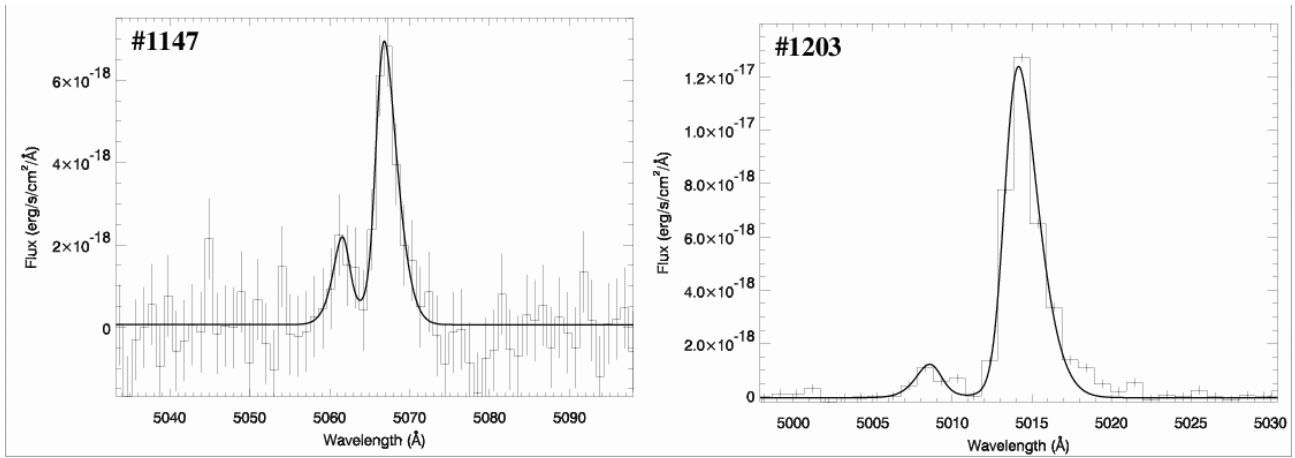


Fig. 16. Spectra of emitter #1147 (left) and #1203 (right).

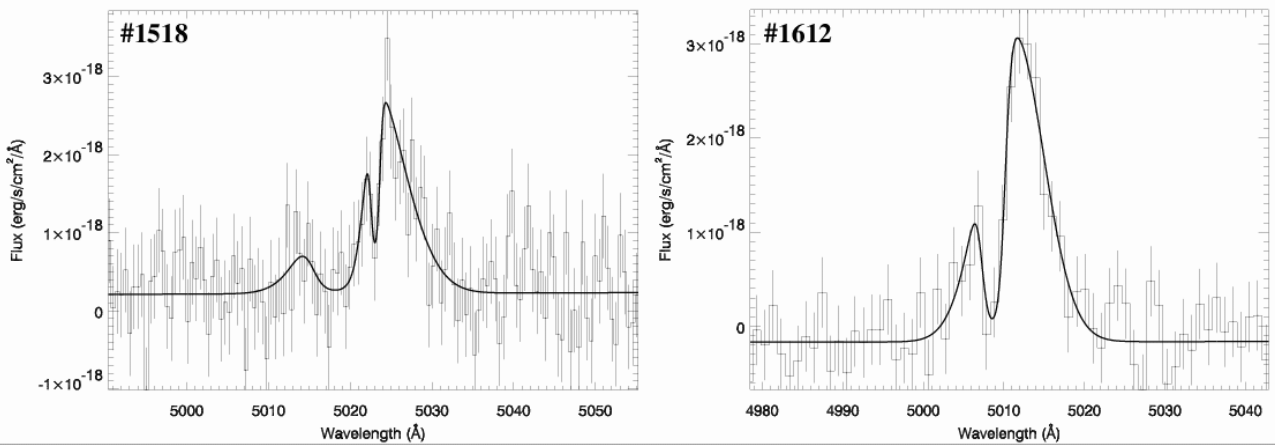


Fig. 17. Spectra of emitter #1518 (left) and #1612 (right).

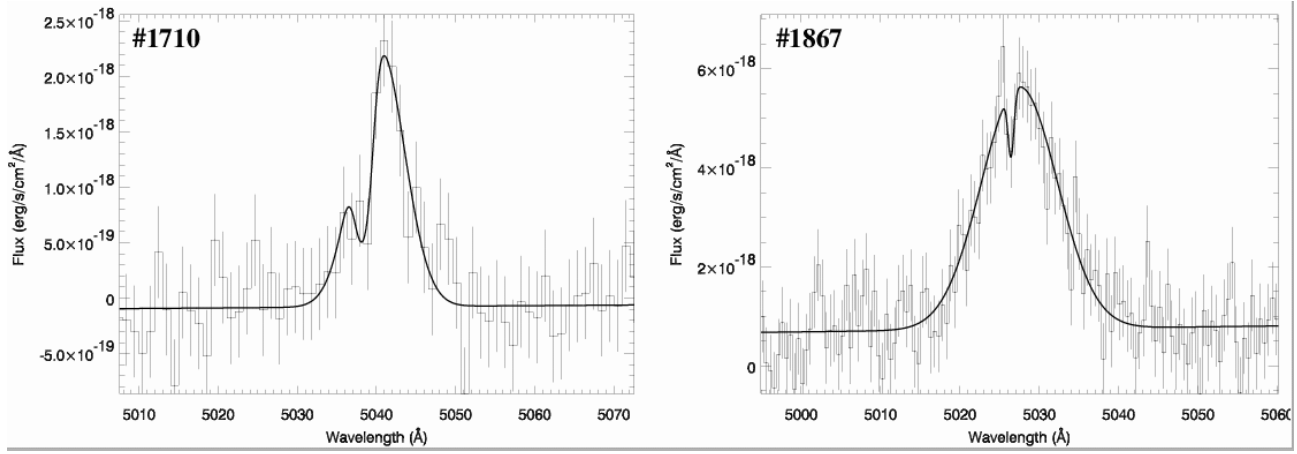


Fig. 18. Spectra of emitter #1710 (left) and #1867 (right).

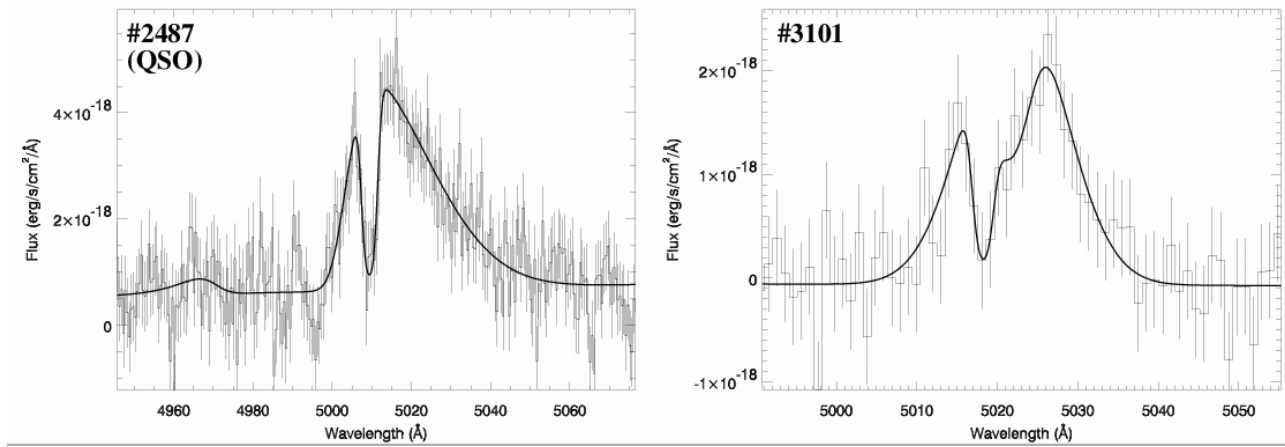


Fig. 19. Spectra of emitter #2487 (left) and #3101 (right).

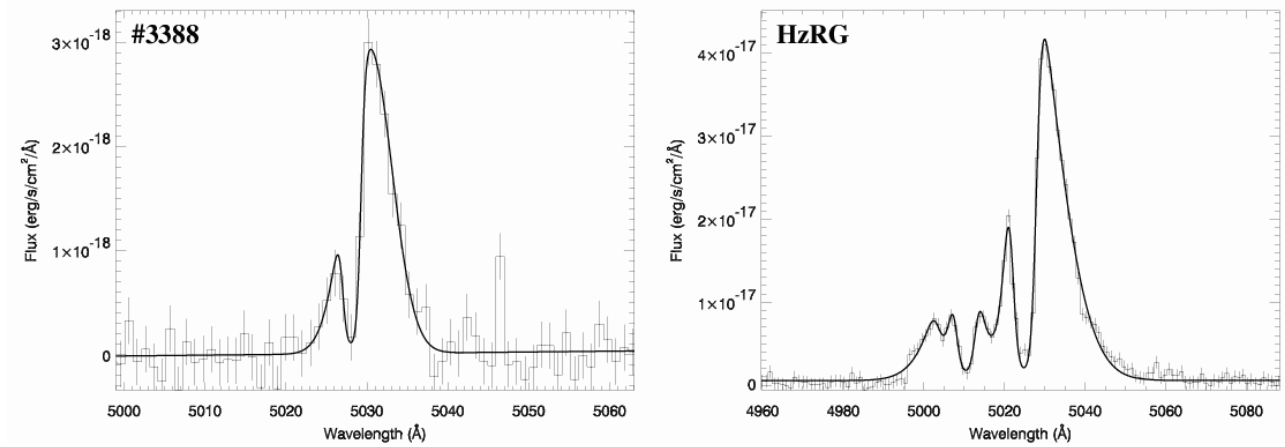


Fig. 20. Spectra of emitter #3388 (left) and HzRG (right).